



# Opposing trends in the peak and low ozone concentrations in eastern China: anthropogenic and meteorological influences

Zhuang Wang<sup>1,2</sup>, Chune Shi<sup>1,2</sup>, Hao Zhang<sup>1,2</sup>, Xianguang Ji<sup>8</sup>, Yizhi Zhu<sup>7</sup>, Congzi Xia<sup>10</sup>, Xiaoyun Sun<sup>1,2</sup>, Xinfeng Lin<sup>2</sup>, Shaowei Yan<sup>2</sup>, Suyao Wang<sup>9</sup>, Yuan Zhou<sup>11,12</sup>, Chengzhi Xing<sup>3</sup>, Yujia Chen<sup>1,2</sup>, and Cheng Liu<sup>4,3,5,6</sup>

<sup>1</sup>Anhui Province Key Laboratory of Atmospheric Science and Satellite Remote Sensing, Anhui Institute of Meteorological Sciences, Hefei 230031, China

<sup>2</sup>Shouxian National Climatology Observatory, Huaihe River Basin Typical Farm Eco-meteorological Experiment Field of CMA, Shouxian 232200, China

<sup>3</sup>Key Lab of Environmental Optics and Technology, Anhui Institute of Optics and Fine Mechanics, Hefei Institutes of Physical Science, Chinese Academy of Sciences, Hefei 230031, China

<sup>4</sup>Department of Precision Machinery and Precision Instrumentation, University of Science and Technology of China, Hefei 230026, China

<sup>5</sup>Center for Excellence in Regional Atmospheric Environment, Institute of Urban Environment, Chinese Academy of Sciences, Xiamen 361021, China

<sup>6</sup>Key Laboratory of Precision Scientific Instrumentation of Anhui Higher Education Institutes, University of Science and Technology of China, Hefei 230026, China

<sup>7</sup>School of Environmental Science and Engineering, Suzhou University of Science and Technology, Suzhou 215009, China

<sup>8</sup>Information Materials and Intelligent Sensing Laboratory of Anhui Province, Anhui University, Hefei 230601, China

<sup>9</sup>Huaibei Meteorological Bureau, Huaibei 235000, Anhui, China

<sup>10</sup>Institute of Big Data for Vocational Education, Guangdong Polytechnic of Science and Technology, Zhuhai 519000, China

<sup>11</sup>Jiangxi Ecological Meteorology Center, Nanchang 330096, China

<sup>12</sup>Nanchang National Climate Observatory, Nanchang 330043, China

**Correspondence:** Chengzhi Xing (xingcz@aiofm.ac.cn), Yujia Chen (chenyj18@mail.ustc.edu.cn), and Cheng Liu (chliu81@ustc.edu.cn)

Received: 5 February 2024 – Discussion started: 30 April 2024

Revised: 27 September 2024 – Accepted: 28 October 2024 – Published: 9 January 2025

**Abstract.** Due to considerable reductions in nitrogen oxides (NO<sub>x</sub>), ozone trends and variations in eastern China remain inadequately understood. Long-term observations of ozone precursors were conducted to explore the factors influencing ozone trends in this region. Combined with satellite and surface measurements, we evaluated the trends in low (2nd percentile), typical (50th percentile), and peak (98th percentile) ozone concentrations in detail. Observations indicate a significant decrease in peak ozone concentrations ( $-0.5\% \text{ yr}^{-1}$ ), alongside an increase in low ozone concentrations ( $0.3\% \text{ yr}^{-1}$ ), across eastern China during May–September from 2017 to 2022. The decline in typical ozone concentrations is notably slower than that of peak ozone concentrations, which is approximately  $-0.02 \text{ ppb yr}^{-1}$  ( $-0.0\% \text{ yr}^{-1}$ ) during the same period. Anthropogenic emissions primarily drive trends in low and peak ozone concentrations in eastern China, though meteorological effects also play a role. Ozone formation sensitivity shifts from volatile organic compound (VOC)-limited or transitional regimes in the morning (08:00–11:00 local time, LT), when ozone concentrations rise sharply, to NO<sub>x</sub>-limited

regimes around peak concentrations ( $\sim 14:00$  LT). The reduction in  $\text{NO}_x$  concentrations is identified as a key factor driving the decline in peak ozone concentrations, aiming to further reduce ozone exceedance days. Thus, controlling  $\text{NO}_x$  concentrations emerges as crucial for mitigating peak ozone levels. Moreover, the increase in low ozone concentrations can also be attributed to both anthropogenic emissions and meteorological factors. Our findings underscore the beneficial impacts of  $\text{NO}_x$  reduction on managing peak ozone levels. Regular changes in ozone formation sensitivity throughout the day should be considered when formulating effective ozone control policies.

## 1 Introduction

In recent decades, China's rapid industrialization and urbanization have yielded substantial economic benefits but have also brought about serious environmental challenges (Li et al., 2018; Song et al., 2023; Z. Wang et al., 2023). Air pollutants, notably ozone ( $\text{O}_3$ ; in warm seasons) and fine particulate matter ( $\text{PM}_{2.5}$ ; in cold seasons), have been the primary targets of China's air quality improvement efforts (Zhang and Cao, 2015; Xing et al., 2024, 2022; Wang et al., 2020; Bauwens et al., 2022). To combat this severe air pollution, the Chinese government initiated the Clean Air Action Plan in 2013 (State Council of China, 2013), resulting in significant reductions in most air pollutant concentrations. The  $\text{PM}_{2.5}$  annual average concentrations were reduced by 30 % to 50 % from 2013 to 2018 (Zhai et al., 2019), while nitrogen oxide ( $\text{NO}_x$ ) and carbon monoxide (CO) emissions dropped by 21 % and 23 %, respectively, from 2013 to 2017 (Zheng et al., 2018). However,  $\text{O}_3$  concentrations showed a yearly increase of  $3.3 \pm 4.7 \mu\text{g m}^{-3} \text{ yr}^{-1}$  from 2015 to 2019 (Mousavinezhad et al., 2021). Subsequently, the second phase of the Clean Air Action Plan was launched in 2018 (State Council of China, 2018), focusing on additional controls for  $\text{O}_3$  emissions. Driven by both anthropogenic activities and meteorological patterns, the upward trend in  $\text{O}_3$  levels in eastern China persisted through at least 2019 (K. Li et al., 2020), making the study of  $\text{O}_3$  formation, sources, and trends in densely populated areas a topic of increasing global concern (Y. Wang et al., 2023b).

Ozone forms rapidly in polluted air through the photochemical oxidation of volatile organic compounds (VOCs) in the presence of  $\text{NO}_x$  ( $\text{NO}_x = \text{NO} + \text{NO}_2$ ) (Li et al., 2022; Cooper et al., 2012). Ambient  $\text{O}_3$  concentrations are influenced by various factors, including precursor levels (Y. Wang et al., 2022; Ding et al., 2023), local meteorological conditions (Han et al., 2020), regional transport (Lang et al., 2021; Y. Wang et al., 2023a), and deposition (Wu et al., 2023). Elevated  $\text{O}_3$  levels can have significant impacts on human health, ecosystems, and climate change, leading to substantial economic losses (Guan et al., 2021; Gao et al., 2022). The formation sensitivity of  $\text{O}_3$  (VOC-limited, transition, and  $\text{NO}_x$ -limited regimes) in a region depends on the relative abundance of VOCs and  $\text{NO}_x$  and their competition for OH radicals, highlighting the importance of controlling

both VOCs and  $\text{NO}_x$  to manage  $\text{O}_3$  production and removal effectively (J. Ren et al., 2022). While  $\text{NO}_x$  concentrations have significantly declined in eastern China since 2013 (Lin et al., 2019), anthropogenic VOC emissions continued to increase until 2019 (Zheng et al., 2018; Bauwens et al., 2022).

Numerous studies have investigated the drivers of the increasing  $\text{O}_3$  trend in China over the past decade, particularly from 2013 to 2017 (K. Li et al., 2020; Lu et al., 2020; Liu et al., 2023). Changes in meteorological conditions and anthropogenic emissions have been identified as the primary causes, with observations and models concluding that anthropogenic impacts dominate the increasing trend of summer  $\text{O}_3$  in China. For instance, K. Li et al. (2020) found that the increase in surface  $\text{O}_3$  in the North China Plain (NCP) from 2013 to 2019 was more influenced by changes in emissions ( $1.2 \text{ ppb yr}^{-1}$ ) than meteorological changes ( $0.7 \text{ ppb yr}^{-1}$ ). Additionally, the decrease in  $\text{PM}_{2.5}$ , mainly achieved by reducing the scavenging of hydroxyl ( $\text{HO}_2$ ) radicals on the aerosol surface, has been found to be crucial for the increase in  $\text{O}_3$  (Li et al., 2018). However, the implications of the heterogeneous uptake of  $\text{HO}_2$  radicals remain debated. These studies have largely focused on a single  $\text{O}_3$  indicator, and due to the recent  $\text{NO}_x$  reduction, the reasons for the variations in  $\text{O}_3$  trends in eastern China, particularly the low and peak  $\text{O}_3$  trends, are not fully understood. This poses a significant challenge for controlling  $\text{O}_3$  pollution and developing effective strategies for sustained air quality improvement.

This study aims to address two key issues by combining extensive ground-based and satellite observations (1) to reveal the surface low, typical, and peak  $\text{O}_3$  trends in eastern Chinese cities in recent years and (2) to explore the driving forces behind these trends. First, we report long-term records of surface  $\text{O}_3$  and related parameters observed at urban air quality monitoring sites and by satellites in eastern China, characterizing the trends of low, typical, and peak surface  $\text{O}_3$  concentrations during the warm season (May–September) from 2017 to 2022. Then, a multiple linear regression (MLR) model is used to evaluate the anthropogenic and meteorological contributions to the 98th and 2nd  $\text{O}_3$  percentile trends. Next, secondary formaldehyde (HCHO) and  $\text{NO}_2$  are employed to diagnose the diurnal variations in  $\text{O}_3$  formation sensitivity and investigate the reasons for peak  $\text{O}_3$  concentration trends in the context of current  $\text{NO}_x$  reduction. Finally, we discuss the reasons for the potential increase in low  $\text{O}_3$

concentrations and the sensitivity of peak and low O<sub>3</sub> trends during the study period.

## 2 Materials and methodology

### 2.1 Surface measurements

The densely populated areas in eastern China mainly include the NCP and the middle and lower Yangtze River Plain (MLYRP), which are both vast and economically developed. It is one of the most polluted areas in China (Mousavinezhad et al., 2021). In this study, O<sub>3</sub> trends in 105 cities in eastern China were investigated, and the spatial distribution of 105 cities in eastern China is shown in Fig. 1a. Real-time hourly observed urban O<sub>3</sub>, NO<sub>2</sub>, and CO concentrations in 105 cities in eastern China from 2017 to 2022 were obtained from the open website of the Ministry of Ecology and Environment of China (MEE; <https://www.mee.gov.cn>; last access: 7 January 2024), with the archive at <https://quotsoft.net/air/> (last access: 7 January 2024). As of 31 August 2018, MEE reported concentrations (in  $\mu\text{g m}^{-3}$ ) under standard conditions (273 K; 1013 hPa). The reference status changed to 298 K and 1013 hPa on 1 September 2018. To facilitate the analysis of the long-term series, the mass concentrations ( $\mu\text{g m}^{-3}$ ) of O<sub>3</sub>, NO<sub>2</sub>, and CO at each site were converted to volume mixing ratios (VMRs; ppb) to eliminate the effect of these changes on trend calculations. Data quality control methods and the calculation of daily maximum 8 h O<sub>3</sub> (MDA8 O<sub>3</sub>) concentrations were implemented according to the statistical requirements of the Technical Regulations for Environmental Air Quality Evaluation (Trial) (HJ633–2013). According to the Technical Regulations of the China Ambient Air Quality Index (AQI) (HJ633–2012), a maximum daily 8 h average (MDA8) O<sub>3</sub> concentration greater than 160  $\mu\text{g m}^{-3}$  is defined as O<sub>3</sub> exceedance days; otherwise, it is an O<sub>3</sub> normal day. Note that all times mentioned in this study refer to local time.

### 2.2 MAX-DOAS measurements

There were 3 typical cities selected from the 105 cities in eastern China to be representative and to conduct multi-axis differential optical absorption spectroscopy (MAX-DOAS) observations, namely Hefei, Huaibei, and Tai'an. First, the three cities are located at similar longitudes, with large differences in latitude, transitioning sequentially from south to north (Fig. 1a). Second, the O<sub>3</sub> concentrations of the three cities differed greatly, with Tai'an having a higher surface mean MDA8 O<sub>3</sub> concentration (82.9 ppb), Hefei having a lower surface mean MDA8 O<sub>3</sub> concentration (65.5 ppb), and Huaibei having an intermediate surface mean MDA8 O<sub>3</sub> concentration (74.3 ppb). The three observation stations in Hefei (31.827° N, 117.233° E), Huaibei (33.962° N, 116.805° E), and Tai'an (36.205° N, 117.094° E) are all set up in urban areas, and the observation periods were from 22 December

2020 to 15 May 2023, 12 April 2019 to 27 May 2022, and 15 July 2021 to 15 May 2023, respectively.

The MAX-DOAS employed in this study consisted of a telescope, two spectrometers (UV: is 303–370 nm; VIS: 390–550 nm; temperature stabilized at  $\sim 20^\circ\text{C}$ ), and a computer as the control and data acquisition unit. The telescope elevation angles were set to 1–6, 8, 10, 15, 30, and 90° and controlled by stepper motors. MAX-DOAS measures spectral information to retrieve aerosols and trace gas profiles. The system was operated only during the daytime (08:00–17:00 local time, LT), with a temporal resolution of 15 min and a spatial resolution of 100 m. Because this study focused on surface O<sub>3</sub> formation sensitivity, only the lowest-level data of NO<sub>2</sub> and HCHO VMRs (ppb) were used. Detailed information regarding the MAX-DOAS instrument, measurement procedures, data inversion algorithms, and data quality control can be found in previous studies (Liu et al., 2022b; Wang et al., 2020; Xing et al., 2022).

Ground-based MAX-DOAS and TROPOspheric Monitoring Instrument (TROPOMI) observations were compared to ensure reliability of the data used in this study. Because the satellite overpass was at approximately 13:30 LT, the mean MAX-DOAS results between 13:00 and 14:00 LT were used for comparison. TROPOMI observations were averaged over a range of 0.2° from the ground-based MAX-DOAS station. Comparisons of NO<sub>2</sub> and HCHO tropospheric vertical column densities (VCDs) from the MAX-DOAS and TROPOMI observations are shown in Figs. S1 and S2 in the Supplement. In general, the MAX-DOAS and TROPOMI observations were in good agreement. The Pearson correlation coefficient of monthly averaged NO<sub>2</sub> VCDs is 0.99 ( $P < 0.01$ ), 0.96 ( $P < 0.01$ ), and 0.96 ( $P < 0.01$ ) in Hefei, Huaibei, and Tai'an, respectively, and the Pearson correlation coefficient of monthly averaged HCHO VCDs is 0.88 ( $P < 0.01$ ), 0.77 ( $P < 0.01$ ), and 0.68 ( $P < 0.01$ ) in Hefei, Huaibei, and Tai'an, respectively. Generally, the NO<sub>2</sub> and HCHO VCDs observed by TROPOMI were smaller than those observed by MAX-DOAS, and the difference may be caused by fitting errors, a priori model bias, cloud and aerosols, and spatiotemporal resolution (De Smedt et al., 2021; Dimitropoulou et al., 2020). In addition, the bottom NO<sub>2</sub> concentrations observed by MAX-DOAS were also compared with urban surface NO<sub>2</sub> concentrations measured by MEE (Fig. S3), and the results were also comparable to the comparisons reported in previous studies (Lin et al., 2022; Wang et al., 2020), with Pearson correlation coefficient of 0.74 ( $P < 0.01$ ), 0.66 ( $P < 0.01$ ), and 0.73 ( $P < 0.01$ ) for Hefei, Huaibei, and Tai'an, respectively. Thus, the MAX-DOAS data are reliable. The differences between MAX-DOAS and MEE observations arise from these two components. First, there was a difference in the detection geometries, as the urban NO<sub>2</sub> concentration observed by MAX-DOAS was the result of scanning along a certain direction, whereas the urban NO<sub>2</sub> concentration observed by MEE was sampled in situ. Second, there were some differences in their

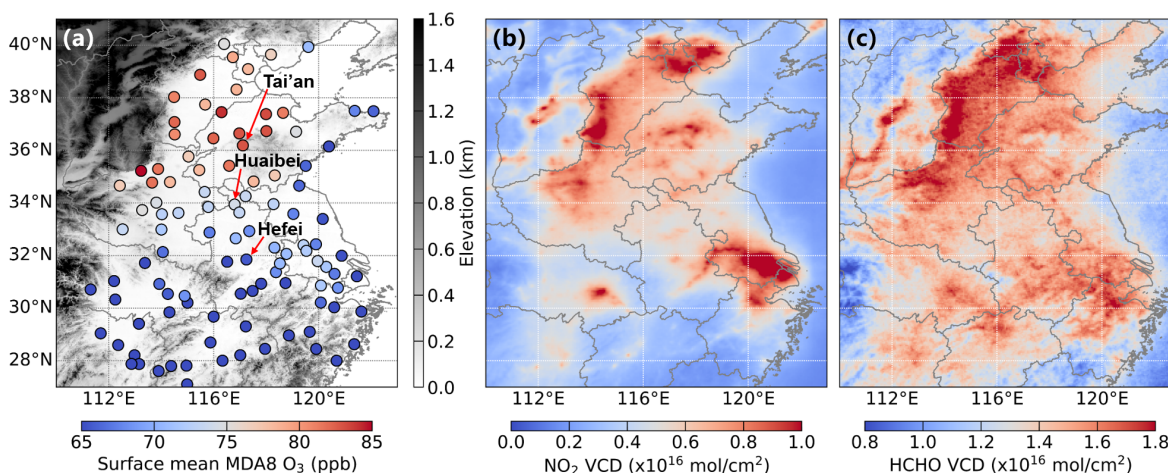


**Figure 1.** Spatial distributions of  $\text{O}_3$  and its precursors in eastern China. (a) Spatial distributions of surface mean MDA8  $\text{O}_3$  concentrations during May–September 2017–2022. The red arrow indicates the name of each city which is equipped with ground-based MAX-DOAS observations. Spatial distributions of tropospheric mean (b)  $\text{NO}_2$  and (c) HCHO VCDs during May–September 2018–2022.

locations, and the urban  $\text{NO}_2$  concentration of the MEE was the average of several in situ observation stations (10, 3, and 3 in Hefei, Huaibei, and Tai’an, respectively), whereas we only used one MAX-DOAS in each city.

### 2.3 Satellite observations

TROPOMI is an imaging spectrometer on board the European Space Agency’s Copernicus Sentinel 5 Precursor satellite launched in October 2017, with a daily overpass of approximately 13:30 LT. TROPOMI has a spatial resolution of  $3.6 \times 7.2$  km (before 6 August 2019) and  $3.6 \times 5.6$  km (after 6 August 2019). A more detailed description of TROPOMI can be found in Veeffkind et al. (2012). The TROPOMI  $\text{NO}_2$  (“S5P\_OFFL\_L2\_NO2...”) and HCHO (“S5P\_OFFL\_L2\_HCHO...”) tropospheric VCD products during May–September 2018–2022 and TROPOMI  $\text{O}_3$  profiles (“S5P\_OFFL\_L2\_O3\_PR...”) during May–September 2022 were used in this study (downloaded from <https://search.earthdata.nasa.gov/search>; last access: 7 January 2024) (Van Geffen et al., 2020; De Smedt et al., 2018). The recommended quality control (QC; in the range of 0–1) filter was applied to exclude HCHO and  $\text{O}_3$  profile retrieval values with QC marks  $< 0.5$ , and  $\text{NO}_2$  retrieval values with QC marks  $< 0.75$ . In addition, the TROPOMI-observed HCHO VCDs and  $\text{NO}_2$  VCDs were regridded to  $0.05 \times 0.05^\circ$  (approximately  $5 \times 5$  km) in this study.

### 2.4 Stepwise multiple linear regression model

To quantify the importance of meteorological drivers, numerous previous studies have used stepwise MLR to derive the relationships between meteorological factors and observed surface  $\text{O}_3$  concentrations in China (Liu et al., 2023; K. Li et al., 2020; Li et al., 2018; Han et al., 2020; X. Zhang

et al., 2023). These studies demonstrated the importance of stepwise MLR in quantifying the contribution of meteorological and anthropogenic components to  $\text{O}_3$  concentrations. We used the same stepwise MLR modeling approach as Zhai et al. (2019), Li et al. (2018), K. Li et al. (2020), Sun et al. (2022), and Liu et al. (2023). Stepwise regressions were performed, adding and removing terms based on their independent statistical significance to obtain the best model fit. Daily meteorological variables were obtained from the ERA5 reanalysis data (downloaded from <https://cds.climate.copernicus.eu>, last access: 7 January 2024) and included temperature ( $T$ ;  $^\circ\text{C}$ ), surface relative humidity (RH; %), total cloud cover (TCC), total precipitation (TP; mm), mean sea level pressure (MSLP; hPa), wind speed of the  $U$  and  $V$  components ( $U$ ;  $V$ ;  $\text{m s}^{-1}$ ), boundary layer height (BLH; m), and vertical velocity at 850 hPa ( $V_{850}$ ;  $\text{m s}^{-1}$ ). Details of the meteorological parameters are presented in Table S1 in the Supplement.

First, we used the MLR model to remove the effects of meteorological variability from 2017 to 2022 according to 98th or 2nd  $\text{O}_3$  percentile trends. The meteorological anomalies  $X_k$  during May–September 2017–2022 were obtained by removing the 6-year means of the 50 d moving averages from the 10 d mean time series. The anomalies calculated in this process were deseasonalized but not detrended. This yields the meteorology-driven 98th or 2nd  $\text{O}_3$  percentile anomalies  $Y_m(t)$ ,

$$Y_m(t) = R + \sum_{k=1}^n \beta_k X_k(t), \quad (1)$$

where  $R$  is the regression constant, and  $\beta_k$  is the regression coefficient. Second, to avoid overfitting, only the three most important meteorological parameters were selected based on their individual contributions to the regressed 98th or 2nd  $\text{O}_3$

percentiles, along with the requirement that they be statistically significant above the 95 % confidence level in the MLR model (Li et al., 2018). The fit results and selected meteorological variables varied by city but were regionally consistent (Tables S2 and S3). The 98th or 2nd O<sub>3</sub> percentile anomalies  $Y_a(t)$  were obtained by deseasonalizing, but not detrending, the 98th or 2nd O<sub>3</sub> percentile time series in a similar manner to that for the meteorological variables (by removing the 6-year means of the 50 d moving averages). The residual anomaly  $Y_r(t)$  after removing the meteorology-driven 98th or 2nd O<sub>3</sub> percentile anomalies from the MLR model is given by

$$Y_r(t) = Y_a(t) - Y_m(t). \quad (2)$$

Finally, the residual is an anomalous component that cannot be explained by the MLR meteorological model and is referred to as meteorologically corrected data by Zhai et al. (2019). It consists of noise due to the limitations of the MLR model and other factors and can be mainly attributed to long-term trends in anthropogenic emission changes over a 6-year period. The trend in the regressed 98th or 2nd O<sub>3</sub> percentile reflected the meteorological contribution, and the residual was then used to reflect the presumed anthropogenic contribution.

## 2.5 Regression model for source separation in primary and secondary HCHO

Tracer-driven linear regression models have been widely used to separate primary and secondary sources of HCHO (Lin et al., 2022; Sun et al., 2021; Hong et al., 2018; Liu et al., 2024; Bao et al., 2022; Heue et al., 2014; MacDonald et al., 2012). CO is emitted directly into the atmosphere through combustion processes (e.g., incomplete combustion in vehicle engines) and can be used as a tracer for primary HCHO emissions (Garcia et al., 2006). O<sub>3</sub> reacts with NO emitted from automobiles to form NO<sub>2</sub>. Therefore, odd amounts of oxygen ( $O_x = O_3 + NO_2$ ) are often used as tracers of photochemical processes in urban atmospheres (Wood et al., 2010). In this study, CO and O<sub>x</sub> were selected as tracers to separate the primary and secondary sources of ambient HCHO, as expressed in Eq. (3) as follows:

$$[\text{HCHO}] = \beta_0 + \beta_1 \times [\text{CO}] + \beta_2 \times [\text{O}_x], \quad (3)$$

where  $\beta_0$ ,  $\beta_1$ , and  $\beta_2$  are regression coefficients and where [HCHO], [CO], and [O<sub>x</sub>] are the ambient HCHO, CO, and O<sub>x</sub> VMRs, respectively.

The relative contributions of the primary, secondary, and atmospheric background HCHO to the total ambient HCHO were calculated from the tracer VMRs and the corresponding

regression coefficients as follows:

$$P_{\text{bg}} = \frac{\beta_0}{\beta_0 + \beta_1 \times [\text{CO}] + \beta_2 \times [\text{O}_x]} \times 100\%, \quad (4)$$

$$P_{\text{pri}} = \frac{\beta_1 \times [\text{CO}]}{\beta_0 + \beta_1 \times [\text{CO}] + \beta_2 \times [\text{O}_x]} \times 100\%, \quad (5)$$

$$P_{\text{sec}} = \frac{\beta_2 \times [\text{O}_x]}{\beta_0 + \beta_1 \times [\text{CO}] + \beta_2 \times [\text{O}_x]} \times 100\%, \quad (6)$$

where  $P_{\text{pri}}$  denotes the contribution of primary sources of HCHO (e.g., vehicular and industrial emissions),  $P_{\text{sec}}$  denotes the contribution of secondary sources of HCHO (photochemical oxidation), and  $P_{\text{bg}}$  denotes the background HCHO. According to previous studies in central and eastern China (Ma et al., 2016; Wang et al., 2015), the background level of HCHO was limited to 1 ppb. Therefore, the regression parameter  $\beta_0$  was fixed at 1 ppb in this study (Hong et al., 2018; Lin et al., 2022). We first perform hourly averaging of HCHO data from MAX-DOAS observations to match CO and O<sub>x</sub> data from MEE observations. Primary and secondary HCHO will then be separated for all available HCHO data from May to September in the MAX-DOAS measurement period. The fitted parameters of the MLR for the measured and modeled HCHO are shown in Fig. S4; it is comparable to the comparisons reported in previous studies (Lin et al., 2022; Sun et al., 2021). As other factors (e.g., meteorological conditions) can also affect the atmospheric HCHO concentration, regression models do not allow us to obtain very consistent results.

## 3 Results and discussions

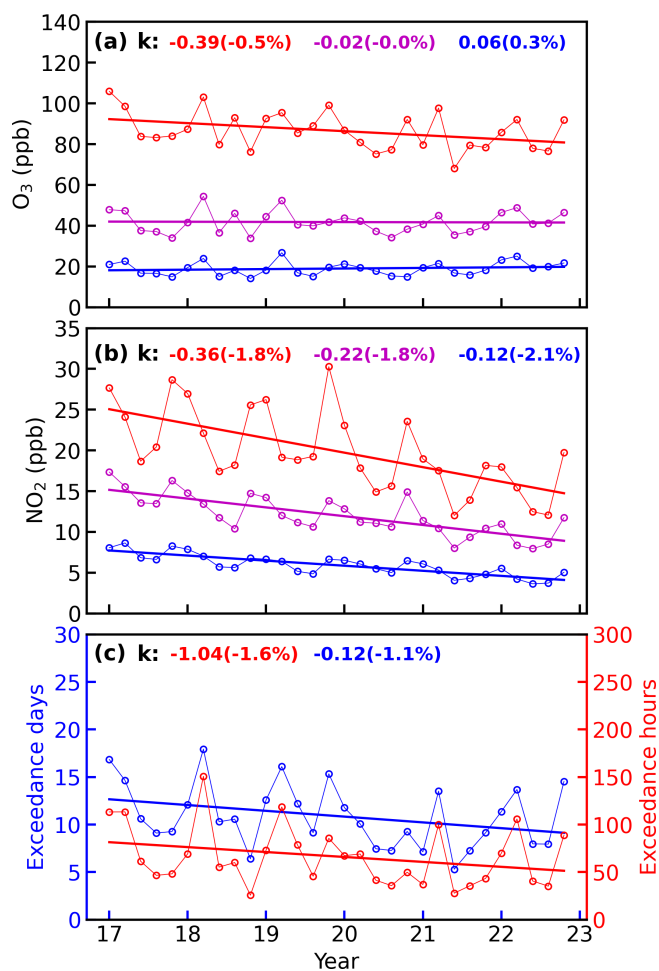
### 3.1 Trends of O<sub>3</sub> and its precursors in eastern China

Figure 1 presents the spatial distribution of the surface mean MDA8 O<sub>3</sub> VMRs at all available urban sites (105 cities in total) in eastern China during May–September of 2017–2022. High MDA8 O<sub>3</sub> VMRs were concentrated in the western cities of eastern China, with the highest values in Jiaozuo of up to 86.4 ppb. High O<sub>3</sub> VMRs indicate intensive anthropogenic emissions of O<sub>3</sub> precursors from these cities, most of which are located in the NCP, which is one of the most polluted areas in China (Li et al., 2018). Figure 1b and c show the average VCDs of NO<sub>2</sub> and HCHO observed by TROPOMI during May–September 2018–2022, respectively. High NO<sub>2</sub> and HCHO levels were clustered mainly in the NCP and MLYRP. In this study, the 2nd, 50th, and 98th percentiles of the hourly O<sub>3</sub> and NO<sub>2</sub> concentrations for cities in eastern China were calculated to determine long-term trends at low, typical, and peak concentration levels, respectively (Cooper et al., 2012; Li et al., 2022; Gaudel et al., 2020). Different percentiles may be related to different influences, such as background concentration levels, emission changes, climate change, and regional transport effects (Lefohn et al., 2010). Li et al. (2014) reported that concentrations below

the 5th, between 25th and 75th, and above 95th percentile represent background, typical, and polluted concentrations, respectively. In principle, the lowest daily O<sub>3</sub> concentrations usually occur before sunrise due to nighttime titration of NO, and the low percentile (2nd percentile) usually characterizes baseline or background conditions because increases in the low O<sub>3</sub> percentile tend to be associated with increases in baseline or background O<sub>3</sub> concentrations. Similar conclusions were also obtained from both models and observations (Jacob et al., 1999; Cynthia Lin et al., 2000). O<sub>3</sub> pollution in eastern China generally occurs in the late afternoon on clear days in the warm season (W. Wang et al., 2022), when the ambient O<sub>3</sub> concentration is highest, so the high percentile (98th) characterizes the conditions of the pollution events. The middle percentiles (25th, 50th, and 75th) usually follow the same trend as the mean values and therefore represent typical conditions (Cooper et al., 2012; Li et al., 2022). Using these indicators to investigate long-term changes in O<sub>3</sub> and NO<sub>2</sub> helps us gain a more detailed understanding through analyses.

As shown in Fig. 2, the 98th O<sub>3</sub> percentile in eastern China showed a significant decreasing trend (about  $-0.39 \text{ ppb yr}^{-1}$ ;  $-0.5 \% \text{ yr}^{-1}$ ) during May–September 2017–2022, and the corresponding O<sub>3</sub> exceedance days ( $-1.1 \% \text{ yr}^{-1}$ ) and exceedance hours ( $-1.6 \% \text{ yr}^{-1}$ ) also dropped. This is in stark contrast to previous studies which have widely observed a rapid increase in average surface O<sub>3</sub> concentrations in Chinese cities, while ignoring changes in their peak concentrations (Lu et al., 2020; Liu et al., 2023; Li et al., 2018, 2021; Chan et al., 2017). The decline rate of the 50th O<sub>3</sub> percentile is considerably slower than that of the 98th O<sub>3</sub> percentile during May–September 2017–2022, which is about  $-0.02 \text{ ppb yr}^{-1}$  ( $-0.0 \% \text{ yr}^{-1}$ ). Unexpectedly, the 2nd O<sub>3</sub> percentile in eastern China showed an increasing trend (about  $0.06 \text{ ppb yr}^{-1}$ ;  $0.3 \% \text{ yr}^{-1}$ ) during May–September 2017–2022; the increase in 2nd O<sub>3</sub> percentile concentrations may be due to the decrease in O<sub>3</sub> titration from fresh NO emissions as NO<sub>x</sub> emissions decrease (Li et al., 2023). It can be confirmed in Fig. 2b that all three NO<sub>2</sub> percentiles (2nd, 50th, and 98th) show a significant decreasing trend during May–September 2017–2022, with relative decreasing trends of  $-2.1 \% \text{ yr}^{-1}$ ,  $-1.8 \% \text{ yr}^{-1}$ , and  $-1.8 \% \text{ yr}^{-1}$ , respectively. Notably, NO<sub>2</sub> declines more rapidly in 2020 and 2021, mainly because of the impact of the COVID-19 pandemic, which has been discussed in detail in previous studies (Liu et al., 2022a). Satellite observations also found a significant decrease in NO<sub>2</sub> concentration in eastern China (Fig. 3a), with a decrease rate of about  $0.09 \times 10^{15} \text{ mol cm}^{-2} \text{ yr}^{-1}$  ( $-1.8 \% \text{ yr}^{-1}$ ). Since 2013, NO<sub>x</sub> emissions have decreased in China owing to a series of air pollution prevention and control policies (Lin et al., 2019; Wang et al., 2019).

We further examined the trends in the 98th and 2nd O<sub>3</sub> percentiles across cities in eastern China from May to September 2017–2022 (Fig. 4). Generally, the trend in low O<sub>3</sub> concentrations in most cities showed an increase, with



**Figure 2.** Trends of surface (a) O<sub>3</sub>, (b) NO<sub>2</sub>, and (c) O<sub>3</sub> exceedance days and O<sub>3</sub> exceedance hours in eastern China during May–September 2017–2022. The solid red, magenta, and blue lines in panels (a) and (b) indicate the trends for the 98th, 50th, and 2nd percentiles, respectively. The labels in panels (a) and (b) represent the trends in O<sub>3</sub> and NO<sub>2</sub> for May–September 2017–2022 (units in ppb per year). The labels in panel (c) represent the trends in O<sub>3</sub> exceedance days and O<sub>3</sub> exceedance hours for May–September 2017–2022. The percentage change is indicated in brackets.

the 2nd O<sub>3</sub> percentile ranging from  $-0.2$  to  $0.5 \text{ ppb yr}^{-1}$  ( $-1.6 \% \text{ yr}^{-1}$  to  $5.6 \% \text{ yr}^{-1}$ ). Conversely, peak O<sub>3</sub> concentrations exhibited a decreasing trend, with the 98th O<sub>3</sub> percentile ranging from  $-1.1$  to  $0.2 \text{ ppb yr}^{-1}$  ( $-1.0 \% \text{ yr}^{-1}$  to  $0.3 \% \text{ yr}^{-1}$ ). The trend in typical O<sub>3</sub> concentrations in eastern China from May to September 2017–2022 ranging from  $-0.4$  to  $0.3 \text{ ppb yr}^{-1}$  ( $-0.8 \% \text{ yr}^{-1}$  to  $0.8 \% \text{ yr}^{-1}$ ), with about one-third of the cities increasing and two-thirds decreasing. The decline in peak O<sub>3</sub> concentrations and the rise in low O<sub>3</sub> concentrations were notably more pronounced in the NCP compared to the MLYRP. The highest increase in low O<sub>3</sub> concentrations was observed in Handan at  $0.5 \text{ ppb yr}^{-1}$ , while the lowest decrease in peak O<sub>3</sub> concentrations was seen

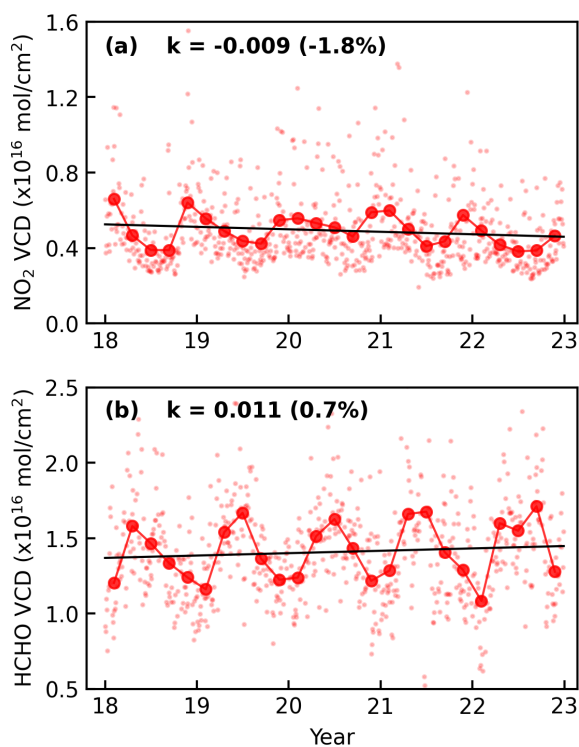


**Figure 3.** Trends of TROPOMI observed in (a)  $\text{NO}_2$  VCDs and (b) HCHO VCD averaged over eastern China during May–September 2018–2022. The labels at the top of each panel represent the trends in  $\text{NO}_2$  VCD and HCHO VCD, respectively. The percentage change is indicated in parentheses. The light red dots in panels (a) and (b) represent the daily values, and the solid red dots are monthly mean values.

in Baoding at  $1.1 \text{ ppb yr}^{-1}$ . Additionally, we investigated the relationship between the trend in mean  $\text{NO}_2$  concentrations and the trend in the 98th  $\text{O}_3$  percentiles from May to September 2017–2022, revealing a significant positive correlation with a Pearson correlation coefficient of  $R = 0.42$  ( $P < 0.01$ ; Fig. 5). In contrast, the trend in the 98th  $\text{NO}_2$  percentile during the same period showed a significant negative correlation with the trend in the 2nd  $\text{O}_3$  percentiles, with a Pearson correlation coefficient of  $R = -0.41$  ( $P < 0.01$ ). Therefore, the substantial reduction in  $\text{NO}_x$  emissions may have had divergent impacts on low and peak  $\text{O}_3$  levels, contributing to the observed decrease in low  $\text{O}_3$  concentrations and increase in peak  $\text{O}_3$  concentrations across urban areas in eastern China.

Due to the absence of long-term ground-based VOCs observations, satellite-observed HCHO VCDs were utilized to indicate VOC variations in eastern China from May to September 2018–2022. HCHO is a transient product reflecting the oxidation of various VOCs, serving as a proxy for VOC emissions, as used in previous studies (Zheng et al., 2018; Zhang et al., 2019). The TROPOMI satellite observations showed a significant upward trend in HCHO VCDs in eastern China during May–September from 2018 to 2022

of approximately  $0.11 \times 10^{15} \text{ mol cm}^{-2} \text{ yr}^{-1}$  ( $0.7 \% \text{ yr}^{-1}$ ) (Fig. 3b). Generally, HCHO VCD exhibits seasonal variability (Li et al., 2021), with higher temperatures and sufficient radiation enhancing photochemical reactions of VOCs and biogenic VOC emissions, thereby promoting HCHO formation (J. Ren et al., 2022). In China, anthropogenic VOC emissions continued to increase until 2019 (Zheng et al., 2018), after which measures were implemented to control them. However, biogenic VOC emissions have been rising in recent years, particularly during extreme heat events such as those experienced in the MLYRP in 2022, leading to a significant increase in biogenic VOC emissions (Zhang et al., 2022; T. Zhang et al., 2023). Importantly, reductions in anthropogenic VOCs have not been sufficient to offset the overall increasing trend in VOC emissions across eastern China (L. Li et al., 2020).

### 3.2 Anthropogenic and meteorological contributions to $\text{O}_3$ trends

The MLR model was applied to assess the significance of the anthropogenic and meteorological components on the 98th and 2nd  $\text{O}_3$  percentile trends. It is worth noting that the aim of this section is not to accurately assess the contribution of each meteorological factor and precursor concentration to  $\text{O}_3$  trends but to explore trends in the 98th and 2nd  $\text{O}_3$  percentile concentrations due to variations in meteorological conditions and anthropogenic emissions in eastern China and to determine the magnitude of the 98th and 2nd  $\text{O}_3$  percentile trends. Based on the daily output of the MLR model, the monthly mean meteorological and anthropogenic components of the 98th and 2nd  $\text{O}_3$  percentiles from May to September 2017–2022 were calculated, and the relative contributions of the meteorological and anthropogenic components to the 98th and 2nd  $\text{O}_3$  percentile trends were quantified. Based on the MLR model, the three key meteorological factors with the most significant effects on the 98th and 2nd  $\text{O}_3$  percentiles were selected (Li et al., 2018; K. Li et al., 2020). The meteorological components of the 98th and 2nd  $\text{O}_3$  percentile concentrations were then simulated using the MLR model driven by the three selected key meteorological factors, and the coefficients of each factor and the Pearson correlation coefficients ( $R$ ) of the fitted MLR model were obtained. The  $R$  for each city in eastern China was in the range of 0.16 to 0.77 for the 2nd  $\text{O}_3$  percentiles (Table S2) and 0.24 to 0.84 for the 98th  $\text{O}_3$  percentiles (Table S3), respectively. RH and  $T$  were the most important factors affecting the 98th and 2nd  $\text{O}_3$  percentile concentrations, followed by TCC, BLH,  $U$ ,  $V$ , and V850 (Tables S2 and S3). These results are consistent with the current understanding of the meteorological effects of  $\text{O}_3$  (Weng et al., 2022; K. Li et al., 2020; Ding et al., 2023).

Figure 6 shows the trends in the monthly mean observed 98th and 2nd  $\text{O}_3$  percentile concentrations, meteorological 98th and 2nd  $\text{O}_3$  percentile components in the MLR simulations, and the residual anthropogenic 98th and 2nd  $\text{O}_3$  per-

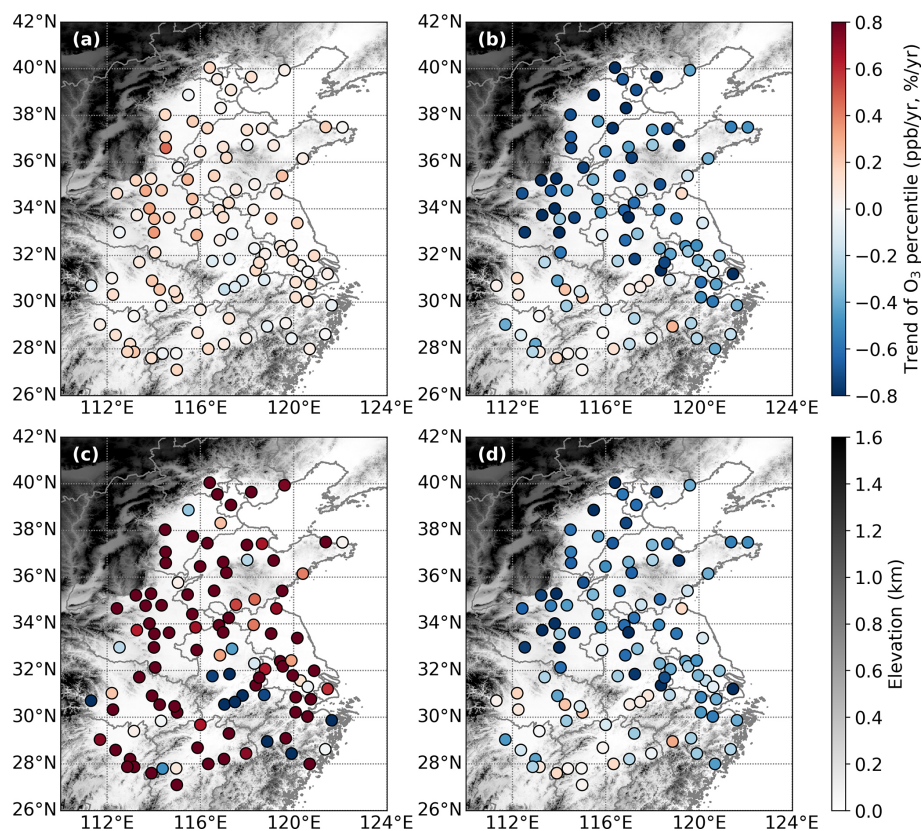


**Figure 4.** Trends of peak and low O<sub>3</sub> concentrations in eastern China. Trend of (a) 2 % and (b) 98 % O<sub>3</sub> percentiles (units in ppb per year), with percentage variations in the (c) 2 % and (d) 98 % O<sub>3</sub> percentile (units in % per year).

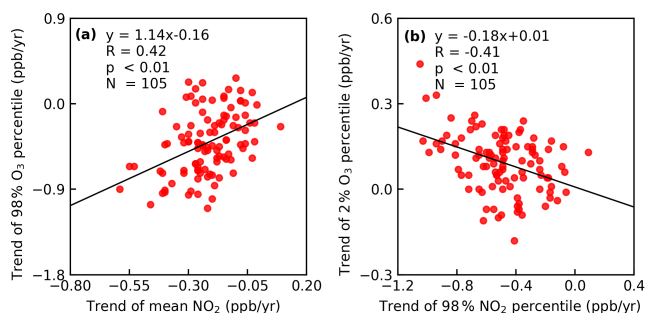


**Figure 5.** Scatterplots showing the relationships between the (a) trend of mean NO<sub>2</sub> concentrations and the trend of the 98th O<sub>3</sub> percentiles, as well as the (b) trend of the 98th NO<sub>2</sub> percentiles and trend of the 2nd O<sub>3</sub> percentiles in each city in eastern China during May–September 2017–2022. The correlation coefficients are shown in the top left of each panel.  $N$  is for the number of cities.

centile components during May–September 2017–2022. The trend of the monthly mean 98th O<sub>3</sub> percentile meteorological component obtained by the MLR model from May to September 2017–2022 was considerably smaller than that of the anthropogenic component, with almost no trend between 2017 and 2022 (0.005 ppb yr<sup>-1</sup>). Meteorological influences

explained only 3 % (0.005 ppb yr<sup>-1</sup>) of the observed 98th O<sub>3</sub> percentile trend during May–September 2017–2022, with the remaining –103 % (–0.183 ppb yr<sup>-1</sup>) determined by anthropogenic influences. However, if we count the monthly mean 98th O<sub>3</sub> percentiles trends from May–September 2017–2021, we find a more significant downward trend in 98th O<sub>3</sub> percentiles (–0.363 ppb yr<sup>-1</sup>), with a contribution of –0.119 ppb yr<sup>-1</sup> (–33 %) from the meteorological component and –0.244 ppb yr<sup>-1</sup> (–67 %) from the anthropogenic component (Table 1). The differences in the O<sub>3</sub> trend statistics for 2017–2022 and 2017–2021 are mainly due to the meteorological conditions in 2022, which will be analyzed in detail in Sect. 4. Separating the observed 2017–2022 98th O<sub>3</sub> percentile trends by month shows that the seasonal May–September trend of –0.178 ppb yr<sup>-1</sup> over eastern China (Table 1) is driven by June, July, and September. The observed trends were –0.020 ppb yr<sup>-1</sup> for May, –4.437 ppb yr<sup>-1</sup> for June, –1.745 ppb yr<sup>-1</sup> for July, –0.687 ppb yr<sup>-1</sup> for August, and 1.999 ppb yr<sup>-1</sup> for September. This month-to-month difference was driven mainly by meteorology. As derived from the MLR model, the meteorologically driven 98th O<sub>3</sub> percentile trends for July and September were –1.100 and 1.136 ppb yr<sup>-1</sup>, respectively, which are larger than those

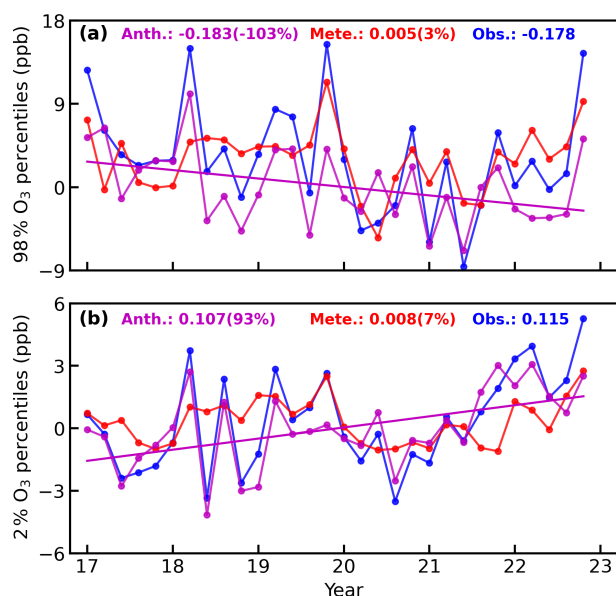


**Figure 6.** Trends of observed (blue lines), meteorological (red lines), and anthropogenic (magenta lines) (a) 98th and (b) 2nd O<sub>3</sub> percentile components in eastern China during May–September 2017–2022. The labels at the top of each panel represent the trend in the observed, meteorological, and anthropogenic components.

of the anthropogenic trend ( $-0.645 \text{ ppb yr}^{-1}$  for July and  $0.863 \text{ ppb yr}^{-1}$  for September).

The trend of the mean 2nd O<sub>3</sub> percentiles meteorological component ( $0.008 \text{ ppb yr}^{-1}$ , 7.0%) was also smaller than that of the anthropogenic component ( $0.107 \text{ ppb yr}^{-1}$ , 93.0%) from May–September 2017–2022. It is worth noting that the increasing trend of the 2nd O<sub>3</sub> percentiles during May–September 2017–2021 was significantly smaller than that during May–September 2017–2022 ( $0.0270.115 \text{ ppb yr}^{-1}$  vs.  $0.115 \text{ ppb yr}^{-1}$ ). The contribution of meteorological components to the 2nd O<sub>3</sub> percentile trends during May–September 2017–2021 was  $-0.044 \text{ ppb yr}^{-1}$  ( $-163.0\%$ ), while the anthropogenic component trend of 2nd O<sub>3</sub> percentiles was  $0.071 \text{ ppb yr}^{-1}$  ( $263.0\%$ ) (Table 1). This indicates that meteorological factors are not conducive to the increasing trend of low O<sub>3</sub> concentrations during May–September 2017–2021 and that the increasing trend of low O<sub>3</sub> concentrations is mainly controlled by anthropogenic influences. In addition, the observed 2017–2022 2nd O<sub>3</sub> percentile trend by month was  $0.322 \text{ ppb yr}^{-1}$  in May,  $0.205 \text{ ppb yr}^{-1}$  in June,  $0.768 \text{ ppb yr}^{-1}$  in July,  $0.371 \text{ ppb yr}^{-1}$  in August, and  $1.290 \text{ ppb yr}^{-1}$  in September. The observed 2017–2022 2nd O<sub>3</sub> percentile trends by month were driven by July and September, while the sign of the 2nd O<sub>3</sub> percentile trends, driven by meteorological and anthropogenic components, was reversed in July ( $-0.177$  vs.  $0.945$ ). Therefore, although anthropogenic emissions are the main driver of opposing trends in peak and low O<sub>3</sub> concentrations in eastern China,

the effect of changes in meteorological components on the 2nd and 98th O<sub>3</sub> percentile trends cannot be ignored.

### 3.3 Diurnal differences in surface O<sub>3</sub> formation sensitivity

To elucidate the reasons for changes in peak, typical, and low O<sub>3</sub> concentrations in the presence of emission reductions in O<sub>3</sub> precursors (a substantial decrease in NO<sub>x</sub> emissions and a slight increase in VOC emissions), it is critical to accurately determine the O<sub>3</sub> formation sensitivity to its precursors, especially at a high temporal resolution. Secondary HCHO and NO<sub>2</sub> were selected as the representative VOCs and NO<sub>x</sub>, respectively (Xue et al., 2022; Hong et al., 2018, 2022; Lin et al., 2022; B. Ren et al., 2022). Surface NO<sub>2</sub> and HCHO VMRs retrieved from ground-based MAX-DOAS observations were used to diagnose the surface-O<sub>3</sub>-formation-sensitive regime. The thresholds for the VOC-limited, transition, and NO<sub>x</sub>-limited regimes were determined based on the correlation between the O<sub>3</sub> concentrations and the changes in the O<sub>3</sub> precursor concentrations under different FNR (defined as the ratio of HCHO VMRs to NO<sub>2</sub> VMRs;  $\text{FNR} = \text{HCHO}/\text{NO}_2$ ). Here, we used  $\text{FNR}_{\text{sec}}$  (defined as the ratio of secondary HCHO to NO<sub>2</sub>;  $\text{FNR}_{\text{sec}} = \text{HCHO}_{\text{sec}}/\text{NO}_2$ ) as an indicator of O<sub>3</sub> formation sensitivity.

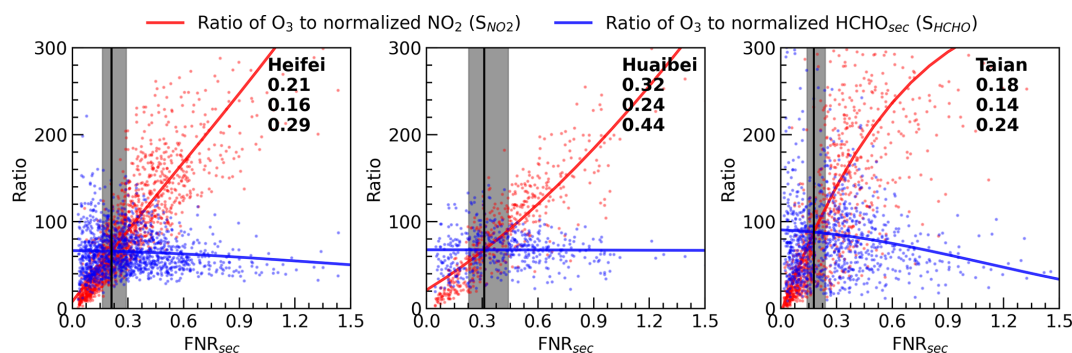
Compared with conventional FNR,  $\text{FNR}_{\text{sec}}$  eliminates the background and primary HCHO interference, improves the accuracy of diagnosing O<sub>3</sub> formation sensitivity, and contributes to a better understanding of O<sub>3</sub> formation sensitivity (Lin et al., 2022; Xue et al., 2022). Most of the  $\text{FNR}_{\text{sec}}$  values ( $\sim 98\%$ ) varied between 0.03 and 1.5 during the whole observations, and excessively low  $\text{FNR}_{\text{sec}}$  values can be attributed to deficiencies in the HCHO source assignment in the MLR model. Therefore,  $\text{FNR}_{\text{sec}}$  values greater than 1.5 (or less than 1.5 up to 0.03) were filtered out for quality control.

Three steps are involved in determining the  $\text{FNR}_{\text{sec}}$  threshold. First, the surface hourly averaged secondary HCHO and NO<sub>2</sub> VMRs during May–September based on MAX-DOAS observations were normalized by dividing their respective mean values because of the large differences in surface HCHO and NO<sub>2</sub> concentrations (Su et al., 2017; B. Ren et al., 2022). The ratio of the hourly averaged O<sub>3</sub> VMRs to the hourly averaged normalized NO<sub>2</sub> VMRs ( $S_{\text{NO}_2}$ ) and the ratio of the hourly averaged O<sub>3</sub> VMRs to the hourly averaged normalized secondary HCHO VMRs ( $S_{\text{HCHO}}$ ) were calculated. Finally, third-order polynomials were used to fit  $S_{\text{NO}_2}$  and  $S_{\text{HCHO}}$  (Fig. 7).

As shown in Fig. 7, the third-order fitting of  $S_{\text{NO}_2}$  increased almost linearly with the  $\text{FNR}_{\text{sec}}$  values, similar to  $S_{\text{HCHO}}$ . When  $S_{\text{NO}_2}$  is significantly larger than  $S_{\text{HCHO}}$ , O<sub>3</sub> formation is more sensitive to NO<sub>x</sub>, which is the NO<sub>x</sub>-limited regime, and vice versa. For example, in Hefei,  $S_{\text{NO}_2}$  and  $S_{\text{HCHO}}$  intersected at  $\text{FNR}_{\text{sec}} = 0.21$ .  $\text{FNR}_{\text{sec}}$  values less

**Table 1.** Observed (Obs.), meteorologically ( Mete.), and anthropogenically (Anth.) driven trends of the 2% and 98% O<sub>3</sub> percentiles in eastern China from 2017 to 2022 and from 2017 to 2021.

	May–September 2017–2022 trends						May–September 2017–2021 trends					
	2 %			98 %			2 %			98 %		
	Obs.	Mete.	Anth.	Obs.	Mete.	Anth.	Obs.	Mete.	Anth.	Obs.	Mete.	Anth.
Total	0.115	0.008	0.107	−0.178	0.005	−0.183	0.027	−0.044	0.071	−0.363	−0.119	−0.244
May	0.322	0.017	0.305	−0.020	−0.661	0.641	−0.438	−0.257	−0.181	−3.702	−0.968	−2.734
June	0.205	−0.032	0.237	−4.437	−1.894	−2.543	−0.364	−0.169	−0.195	−2.645	0.124	−2.769
July	0.768	−0.177	0.945	−1.745	−1.100	−0.645	0.665	−0.247	0.912	−2.974	−2.370	−0.604
August	0.371	0.084	0.287	−0.687	−0.156	−0.531	−0.003	−0.260	0.257	−1.473	−0.908	−0.565
September	1.290	0.319	0.971	1.999	1.136	0.863	0.884	−0.126	1.010	1.352	0.814	0.538

**Figure 7.** Third-order fitting of ratios of O<sub>3</sub> VMRs versus normalized NO<sub>2</sub> VMRs and ratios of O<sub>3</sub> VMRs versus normalized secondary HCHO VMRs in different FNR<sub>sec</sub> values in Hefei, Huaibei, and Tai'an during May–September, based on MAX-DOAS observations. The intersect at FNR<sub>sec</sub> is indicated by the solid black line. The vertical shadow indicates the relative difference between the ratios of O<sub>3</sub> VMRs versus the normalized NO<sub>2</sub> VMRs and ratios of O<sub>3</sub> VMRs versus secondary HCHO VMRs within 25% (transition regime). The labels at the top right of each panel represent the intersect FNR<sub>sec</sub> values and the thresholds for the NO<sub>x</sub>-limited regime (high) and VOC-limited regime (low) in Hefei, Huaibei, and Tai'an, respectively.

than 0.16 and greater than 0.29 correspond to the VOC-limited regime and NO<sub>x</sub>-limited regime, respectively, where the relative difference between  $S_{\text{NO}_2}$  and  $S_{\text{HCHO}}$  is more than 25% (Lin et al., 2022), and the range of FNR<sub>sec</sub> values from 0.16 to 0.29 represents a transition regime. For Huaibei and Tai'an, the transition regime range was 0.24–0.44 and 0.14–0.24, respectively. The FNR<sub>sec</sub> threshold for O<sub>3</sub> formation sensitivity varies in different cities, which may be due to differences in O<sub>3</sub> precursor emissions.

Figure 8 shows the diurnal variations in O<sub>3</sub> and its precursors at three stations (Hefei, Huaibei, and Tai'an) in eastern China, from south to north. O<sub>3</sub> and NO<sub>2</sub> VMRs showed diametrically opposite trends from 08:00 to 13:00 LT, with O<sub>3</sub> concentrations rapidly increasing (about 8.2, 7.4, and 8.6 ppb h<sup>−1</sup> in Hefei, Huaibei, and Tai'an, respectively) and NO<sub>2</sub> concentrations gradually decreasing (about −0.90, −0.86, and −1.49 ppb h<sup>−1</sup> in Hefei, Huaibei, and Tai'an, respectively). Ambient HCHO concentrations depend on the primary emissions and photo-oxidation of VOCs (Xue et al., 2022). We separated the primary and secondary sources of HCHO using the CO and O<sub>x</sub> VMRs, and their diurnal variations are shown in Fig. 8d–f. The primary source con-

tributed the most to the ambient HCHO concentration. Atmospheric primary HCHO concentrations are mainly derived from motor vehicle exhaust fumes, the petrochemical industry, solvent use, and combustion emissions (Ma et al., 2019). Hefei, Huaibei, and Tai'an are located in the NCP, which is the region with the highest primary emissions of air pollutants in China (Li et al., 2017). The rapid industrialization and urbanization in these developing cities has influenced the primary and secondary HCHO concentrations, and HCHO mainly stems from initial atmospheric pollutants (Lu et al., 2024). The HCHO from primary emissions was highest between 08:00 and 10:00 LT (about 2.63, 2.50, and 4.30 ppb in Hefei, Huaibei, and Tai'an, respectively) and then gradually decreased, reaching the lowest concentration around 15:00 LT with about 1.78, 1.54, and 1.82 ppb in Hefei, Huaibei, and Tai'an, respectively, gradually rising thereafter. High primary HCHO concentrations in the morning and evening may have been due to emissions from traffic (Hong et al., 2018; Zhang and Cao, 2015). Secondary HCHO concentrations were lowest in the morning, at about 0.58, 0.84, and 0.65 ppb in Hefei, Huaibei, and Tai'an, respectively; with the enhancement of photochemical reactions and the resump-

tion of human activities, the secondary HCHO concentrations gradually increased from 08:00 to 12:00 LT, and the first peak usually occurred at 11:00–14:00 LT. The proportion of secondary HCHO VMRs in the total HCHO VMRs also increased rapidly, and the proportion of secondary HCHO VMRs in the total HCHO VMRs gradually stabilized after 12:00 LT, with about 24 %, 31 %, and 22 % in Hefei, Huaibei, and Tai'an, respectively. Similar diurnal variation trends were found in Shenyang (Xue et al., 2022), Nanjing (Hong et al., 2018), Guangzhou (Lin et al., 2022), Shenzhen (Zhang and Cao, 2015), Rome (Possanzini et al., 2002), and Toyama (Taguchi et al., 2020), etc. It is worth noting that the secondary HCHO VMRs in Hefei, Huaibei, and Tai'an increased significantly between 16:00 and 17:00 LT; however, the specific reasons remain to be further investigated. In general, NO<sub>2</sub> concentrations were higher, and secondary HCHO concentrations were lower, in the early morning; with the enhancement of photochemical reactions (08:00–13:00 LT), NO<sub>2</sub> concentrations decreased rapidly, and secondary HCHO concentrations increased gradually.

The significant diurnal variation in O<sub>3</sub> precursors contributes to the transition of O<sub>3</sub> formation sensitivity, as indicated by the FNR<sub>sec</sub>, demonstrating a distinct single-peak pattern. As shown in Fig. 8j–l, FNR<sub>sec</sub> increases sharply from 08:00 to 13:00 LT, corresponding with considerable increases in O<sub>3</sub> VMRs. In cities like Hefei, Huaibei, and Tai'an, O<sub>3</sub> formation sensitivity starts in the VOC-limited regime (below the shaded area) at 08:00–09:00 LT, gradually transitioning to the transition regime by 10:00–11:00 LT. By 12:00–14:00 LT, O<sub>3</sub> formation in Huaibei predominantly enters the NO<sub>x</sub>-limited regime before shifting back to the transition regime after 15:00 LT. Similarly, in Hefei and Tai'an, the NO<sub>x</sub>-limited regime prevails from 12:00 to 16:00 LT, shifting towards the transition regime after 17:00 LT. Overall, O<sub>3</sub> formation sensitivity is VOC-limited or transition regime dominant during periods of rapid O<sub>3</sub> concentration increases (08:00–12:00 LT), shifting to transition or NO<sub>x</sub>-limited regimes when O<sub>3</sub> concentrations peak (12:00–14:00 LT). We further investigated the diurnal characteristics of FNR<sub>sec</sub> on O<sub>3</sub> exceedance days (MDA8 O<sub>3</sub> > 160 µg m<sup>-3</sup>). Compared to the entire observation period, FNR<sub>sec</sub> on O<sub>3</sub> exceedance days exhibits a faster transition from 08:00 to 13:00 LT and prolonged persistence in the NO<sub>x</sub>-limited regime.

The diurnal variation in the O<sub>3</sub> VMRs was very similar to that of FNR<sub>sec</sub>, particularly from 08:00 to 13:00 LT, and both increased sharply. The exponential function was applied to fit the relationship between the O<sub>3</sub> concentration and FNR<sub>sec</sub> values from 08:00 to 13:00 LT in Hefei, Huaibei, and Tai'an (Fig. 9), and all three cities showed significant positive correlations, with Pearson correlation coefficients of 0.53 ( $P < 0.01$ ), 0.40 ( $P < 0.01$ ), and 0.52 ( $P < 0.01$ ) in Hefei, Huaibei, and Tai'an, respectively. Moreover, the exponential fitting is better on the O<sub>3</sub> exceedance days, and the correlation coefficients are higher, with 0.69 ( $P < 0.01$ ),

0.59 ( $P < 0.01$ ), and 0.61 ( $P < 0.01$ ) in Hefei, Huaibei, and Tai'an, respectively. This indicates that the dependence of the O<sub>3</sub> production rate on its precursors rapidly shifts with increasing O<sub>3</sub> concentration, particularly on O<sub>3</sub> exceedance days. These changes also suggest that the dependence of O<sub>3</sub> on its precursors is extremely complex, and the precise control of O<sub>3</sub> pollution requires the identification of O<sub>3</sub> formation sensitivity mechanisms with high temporal resolution and targeted control of O<sub>3</sub> precursor concentrations.

Owing to the limitations of the observational data, the analysis of diurnal transitions in surface O<sub>3</sub> formation sensitivity is limited to three cities in eastern China. Here, other cities in eastern China were further investigated using satellite observations, and we construct conventional FNR using TROPOMI-observed NO<sub>2</sub> and HCHO VCDs from May to September 2018–2022. In order to avoid the misjudgment of O<sub>3</sub> formation sensitivity caused by arbitrary selection of FNR thresholds, a third-order polynomial model was applied to investigate the empirical relationship between TROPOMI FNR and surface O<sub>3</sub> VMRs, which has been widely used in other studies (J. Ren et al., 2022). Since the TROPOMI-observed surface O<sub>3</sub> VMRs can be obtained after November 2021 in China, we only collected the relationship between TROPOMI FNR and surface O<sub>3</sub> VMRs from May to September, 2022. The third-order polynomial fitting relationship between surface O<sub>3</sub> VMRs and TROPOMI FNR is shown in Fig. 10a, assuming that the peak of the curve (with a slope of zero) marks the transition from the VOC-limited regime to the NO<sub>x</sub>-limited regime; the transition regime is defined as a range of slopes between  $-3$  and  $+3$  (J. Ren et al., 2022). Through the third-order polynomial model, the TROPOMI FNR threshold in eastern China was determined, which are FNR < 2.1 for a VOC-limited regime and FNR > 3.2 for a NO<sub>x</sub>-limited regime.

Figure 11 shows the occurrence probabilities of the VOC-limited regime, transition-limited regime, and NO<sub>x</sub>-limited regime spatial distributions derived from TROPOMI observations in eastern China during May–September 2018–2022. Since the TROPOMI satellite usually transits around 13:30, it can represent the spatial distribution of midday O<sub>3</sub> formation sensitivity in eastern China. Apparently, the midday O<sub>3</sub> formation sensitivity of most cities in eastern China is under a NO<sub>x</sub>-limited regime; only several cities in the northern part of the NCP and Yangtze River Delta are mainly controlled by VOC-limited regime. In addition, Fig. 10b–d show the trend of the area proportion of VOC-limited regime, transition regime, and NO<sub>x</sub>-limited regime in eastern China, where the area proportion of the VOC-limited regime and transition regime decreases at a rate of 0.62 % yr<sup>-1</sup> and 0.18 % yr<sup>-1</sup>, respectively, while the NO<sub>x</sub>-limited regime area proportion increased at a rate of 0.80 % yr<sup>-1</sup>. More importantly, although there is a significant monthly variation in the area proportion of O<sub>3</sub> formation sensitivity, it is usually below 50 % in May and September and below 25 % in June–August; that is, the NO<sub>x</sub>-limited regime dominates the midday O<sub>3</sub> forma-

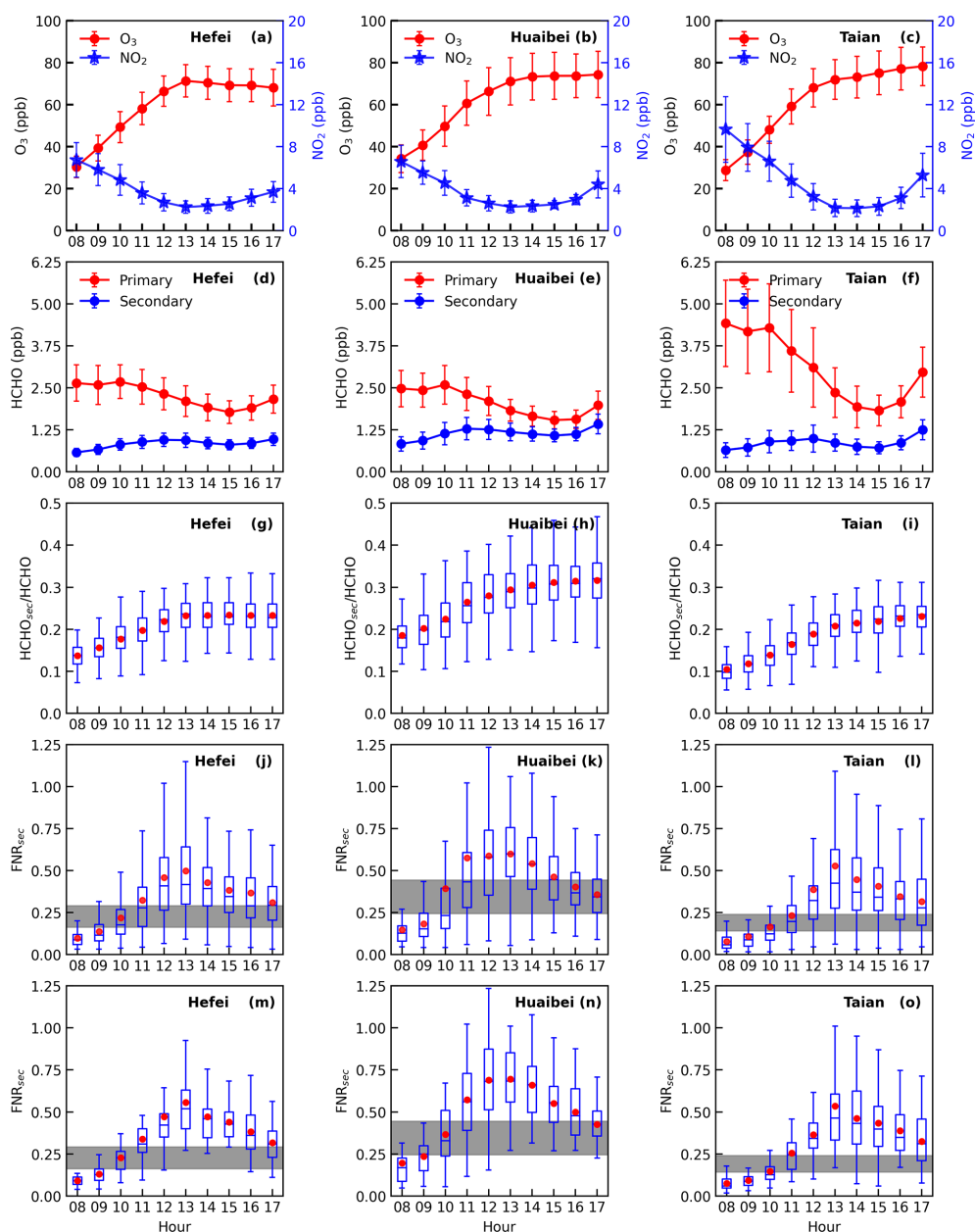


**Figure 8.** Diurnal variation in surface (a–c) O<sub>3</sub> and NO<sub>2</sub> VMRs. (d–f) HCHO VMRs contributed by primary and secondary sources. (g–i) The ratio of secondary HCHO to total HCHO VMRs. (j–l) FNR<sub>sec</sub> during the whole observation. (m–o) FNR<sub>sec</sub> during O<sub>3</sub> exceedance day in Hefei, Huaibei, and Tai’an during May–September, respectively. The vertical bars in panels (a)–(f) represent 1 standard deviation. The dot within the box indicates the mean value, and the positions of box plots represent the 5th, 25th, 50th, 75th, and 95th percentiles, respectively. The horizontal shadow in panels (j)–(o) represents the transition regime; the top of the shadow represents the NO<sub>x</sub>-limited regime, and the bottom of the shadow represents the VOC-limited regime.

tion sensitivity in eastern China. Due to China’s strict control of NO<sub>x</sub> emissions in recent years, the surface O<sub>3</sub> formation sensitivity in many areas of China has shown a transition from the VOC-limited regime to the transition regime or NO<sub>x</sub>-limited regime.

In conclusion, significant diurnal transitions in surface O<sub>3</sub> formation sensitivity primarily stem from fluctuations in

O<sub>3</sub> precursors. Early-morning conditions (08:00–09:00 LT) are mainly a VOC-limited regime; this shifts to a NO<sub>x</sub>-limited regime by midday (12:00–14:00 LT). In addition, the area proportion of VOC-limited regime was also declining, while the NO<sub>x</sub>-limited regime area proportion was increasing. Consequently, the substantial reduction in NO<sub>x</sub> emissions across eastern China has led to pronounced opposite

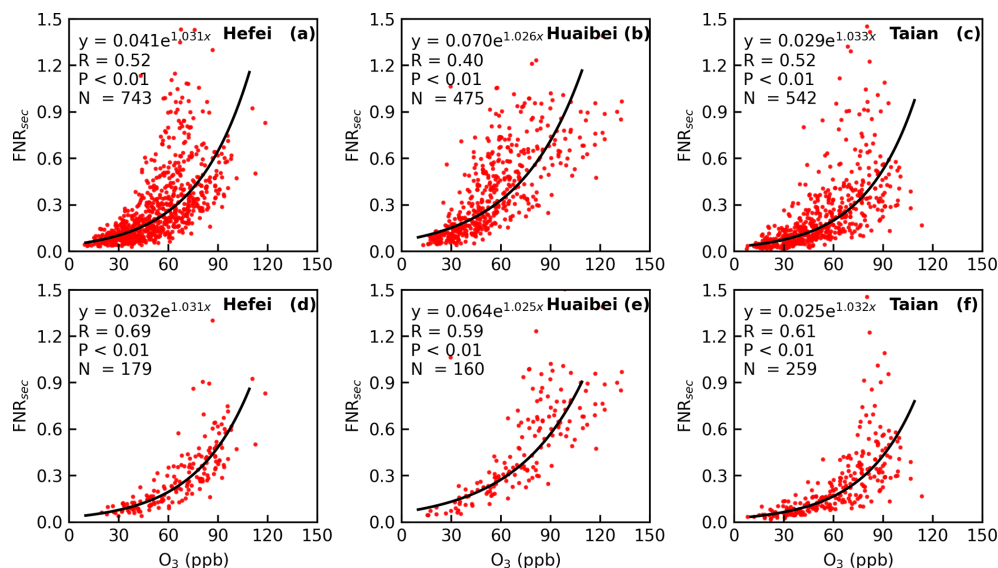


**Figure 9.** The relationship between the  $O_3$  VMRs and  $FNR_{sec}$  during (a–c) the whole observation, and (d–f) the  $O_3$  exceedance day from 08:00 to 13:00 LT in Hefei, Huaibei, and Tai'an, respectively. The black line represents the exponential fitting ( $f(x) = A \times e^B \times x$ ). The fitting functions and correlation coefficients for exponential fit are shown at the top left of each panel.  $N$  is the number of samples.

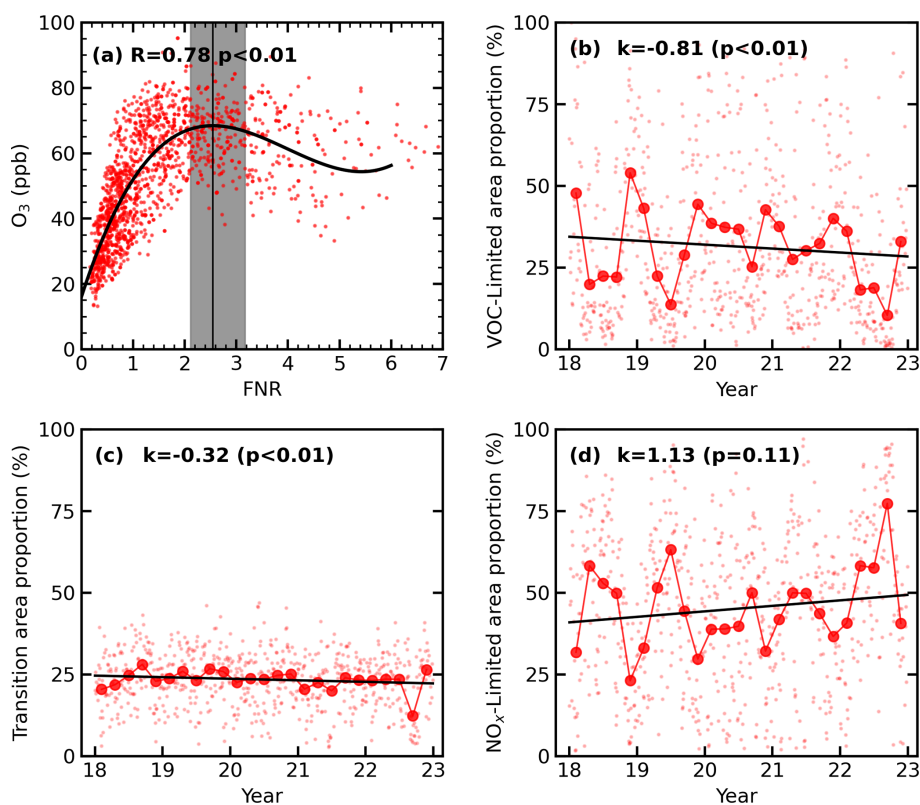


**Figure 10.** (a) Variation in monthly mean  $O_3$  VMRs ( $\sim 13:30$ ) with monthly mean TROPOMI FNR in eastern China during May–September 2022. The solid line represents third-order polynomial fitting. The vertical line represents the maximum value of the fitted curve, and the vertical shadow represents the range of the curve slope from  $-3$  to  $+3$  (transition regime). Trends of TROPOMI observed area proportion for the (b) VOC-limited regime, (c) transition regime, and (d)  $NO_x$ -limited regime over eastern China during May–September 2018–2022. The light red dots in panels (b)–(d) represent the daily values, and the solid red dots are monthly mean values.

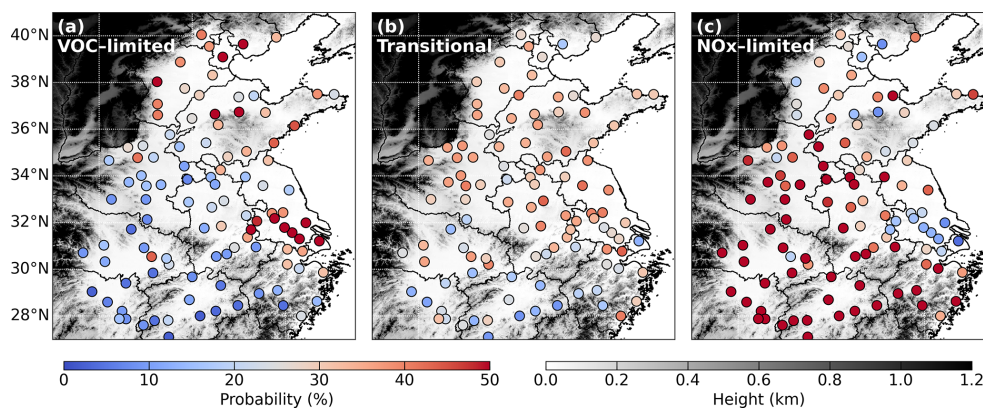


**Figure 11.** Occurrence probabilities of the (a) VOC-limited regime, (b) transition-limited regime, and (c)  $\text{NO}_x$ -limited regime spatial distributions in eastern China derived from TROPOMI observations during May–September 2018–2022.

trends in the low (increased) and peak (decreased) surface  $\text{O}_3$  concentrations, and the surface  $\text{O}_3$  formation sensitivity to VOCs is generally weakened year by year. Accordingly, the  $\text{O}_3$  improvements and benefits of VOC emission reductions may become weaker, while the  $\text{O}_3$  improvements and benefits of  $\text{NO}_x$  emission reductions become larger. Furthermore, the long-distance transport of VOCs has a diminished impact on  $\text{O}_3$  concentrations due to chemical losses from OH radical oxidation during transport, highlighting  $\text{NO}_x$  emission reductions as pivotal for intercity and even long-distance efforts to mitigate regional  $\text{O}_3$  pollution (Y. Wang et al., 2023a).

#### 4 Discussions

Previous analyses have shown that the trend of low  $\text{O}_3$  concentrations in eastern China is increasing, whereas the trend of peak  $\text{O}_3$  concentrations is decreasing. The opposite trend is mainly driven by anthropogenic emissions. Significant  $\text{NO}_x$  emission reductions dominate the reduction in peak  $\text{O}_3$  concentrations in eastern China, owing to the diurnal transition in surface  $\text{O}_3$  formation sensitivity. The discussion focuses on the reasons for the differences in the  $\text{O}_3$  trend statistics for 2017–2022 and 2017–2021 and the reasons for the possible increase in nighttime  $\text{O}_3$ .

As described in Sect. 3.2, the trends for the monthly mean observed, meteorological, and anthropogenic 98th  $\text{O}_3$  percentile concentrations during May–September 2017–2021 are  $-0.363 \text{ ppb yr}^{-1}$ ,  $-0.119 \text{ ppb yr}^{-1}$  ( $-33\%$ ), and  $-0.244 \text{ ppb yr}^{-1}$  ( $-67\%$ ), respectively (Table 1), and the trends for the monthly mean observed, meteorological, and anthropogenic 2nd  $\text{O}_3$  percentile concentrations are  $0.027 \text{ ppb yr}^{-1}$ ,  $-0.044 \text{ ppb yr}^{-1}$  ( $-163\%$ ),  $0.071 \text{ ppb yr}^{-1}$  ( $263\%$ ), respectively. However, the trends of monthly mean observed, meteorological, and anthropogenic 98th  $\text{O}_3$  percentiles during May–September 2017–2022 are  $-0.178 \text{ ppb yr}^{-1}$ ,  $0.005 \text{ ppb yr}^{-1}$  ( $3\%$ ), and

$-0.183 \text{ ppb yr}^{-1}$  ( $-103\%$ ), respectively, and the trends of the observed, meteorological, and anthropogenic 2nd  $\text{O}_3$  percentiles during May–September 2017–2022 are  $0.115 \text{ ppb yr}^{-1}$ ,  $0.008 \text{ ppb yr}^{-1}$  ( $7\%$ ), and  $0.107 \text{ ppb yr}^{-1}$  ( $93\%$ ), respectively. Although anthropogenic emissions dominated variations in  $\text{O}_3$  trends (May–September 2017–2022 and May–September 2017–2021), meteorological effects on  $\text{O}_3$  trends cannot be ignored, particularly in 2022. Shadowed by mid-latitude atmospheric circulation, tropical sea–air coupling, and local land–air feedback processes, a record-breaking super-heat-wave event occurred in most cities in eastern China in the summer of 2022, and some cities broke their highest temperature records (T. Zhang et al., 2023; Zhang et al., 2022). The most important meteorological variables in the MLR model were daily maximum temperature and RH (Tables S2 and S3). The temperature in eastern China showed that the monthly mean nighttime (daytime) temperature in June–August 2022 was  $1.0^\circ$  ( $1.1^\circ$ ),  $0.8^\circ$  ( $1.4^\circ$ ), and  $2.2^\circ$  ( $2.8^\circ$ ) higher than the monthly mean nighttime (daytime) temperature in June–August 2021, respectively (Fig. 12). The monthly mean nighttime (daytime) RH in eastern China in 2022 was  $3.2\%$  ( $3.1\%$ ),  $1.9\%$  ( $4.5\%$ ), and  $9.4\%$  ( $11\%$ ) lower than the monthly mean nighttime (daytime) RH in June–August 2021, respectively. Li et al. (2024) revealed that a sustained heat wave of extremely hot and dry summers in 2022 accelerated photochemical  $\text{O}_3$  production by increasing anthropogenic and biogenic emissions and exacerbated  $\text{O}_3$  accumulation by inhibiting dry deposition due to water-starved vegetation, resulting in an increase in  $\text{O}_3$  pollution by more than  $30\%$  in urban areas. Our results also showed an increase in the meteorological components in the 98th and 2nd  $\text{O}_3$  percentiles in 2022 relative to the meteorological components in the 98th and 2nd  $\text{O}_3$  percentiles in 2021 (Fig. 6). Therefore, extremely hot and dry weather in 2022 will increase the peak and low  $\text{O}_3$  concentrations in eastern China, which is probably the main reason for the difference between the May and Septem-

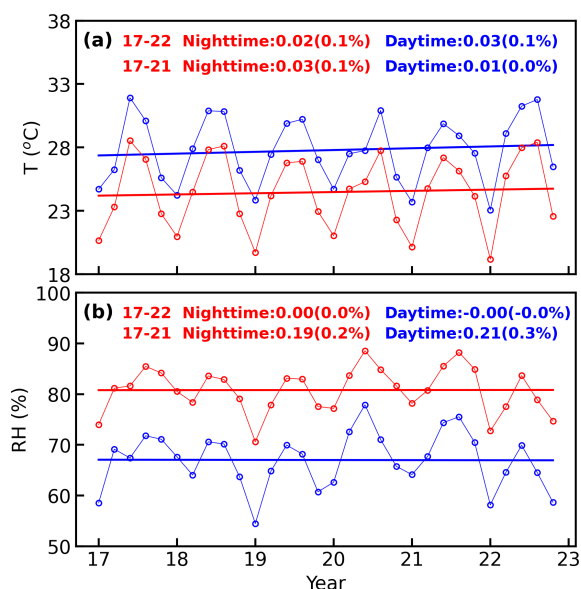


**Figure 12.** Daytime (07:00–19:00 LT) and nighttime (19:00–07:00 LT) (a)  $T$  and (b) RH trends in ERA5 reanalysis data in eastern China during May–September 2017–2022 and May–September 2017–2021. The labels at the top right of each panel represent the trend of  $T$  and RH in eastern China during May–September 2017–2022 and May–September 2017–2021.

ber 2017–2021 and May–September 2017–2022 meteorological component trends.

Overall, meteorological conditions affected  $O_3$  concentrations in three ways. The first is the effect on the photochemical reaction rates (Bloomer et al., 2009), which are affected by rising temperatures and increasing solar radiation intensity, leading to higher- $O_3$  concentrations. Second, the effect on  $O_3$  precursors; high temperature promotes an increase in VOC emissions from land surface vegetation (Churkina et al., 2017), which further leads to an increase in the  $O_3$  concentration. However, favorable meteorological conditions, such as high wind speed and precipitation, can reduce the  $O_3$  precursor concentrations (Mousavinezhad et al., 2021), thereby reducing the  $O_3$  concentration. Finally, transmission and regional transport also affect the distribution of  $O_3$  in cities (Lang et al., 2021). However, the frequency of extreme weather events such as the super-heat-wave event in 2022 is increasing (Jin et al., 2021) in eastern China. In the context of the current warming climate, heat waves of extremely hot and dry conditions can elevate  $O_3$  concentrations by increasing photochemical rates and promoting natural emissions (e.g., soil emissions of  $NO_x$  and vegetation emissions of VOCs), and meteorological components may have an increasing influence on  $O_3$  trends.

Figure 6b shows that the observed increase in the 2nd  $O_3$  percentile was mainly concentrated after 2020 with up to  $0.44 \text{ ppb yr}^{-1}$ . The meteorological components did not change significantly in 2020 and 2021 but considerably in-

creased in 2022, with a trend of  $0.17 \text{ ppb yr}^{-1}$  2020–2022. This rapid increase in the 2nd  $O_3$  percentile is mainly caused by anthropogenic emissions, with a trend of  $0.27 \text{ ppb yr}^{-1}$  for 2020–2022. Owing to the impact of the COVID-19 pandemic, the decrease in  $NO_x$  concentrations was most significant in 2020–2022 (Fig. 2b), and the substantial reduction in  $NO_x$  concentrations weakened the  $O_3$  titration of NO, resulting in an increase in nighttime  $O_3$  concentrations, which was also confirmed by the significant negative correlation between the trend of the 98th  $NO_2$  percentile and the trend of the 2nd  $O_3$  percentile during May–September 2017–2022 (Fig. 5b). A recent study showed that nighttime  $O_3$  depletion in China is mainly caused by the wet-scavenging effect and  $O_3$  titration from fresh NO emissions (Li et al., 2023). The wet-scavenging effect was similar to the effect of precipitation; the higher the ambient humidity, the more conducive it was to  $O_3$  depletion. The RH at night increased slowly in eastern China during May–September of 2017–2021 (Fig. 12b), and the nighttime RH in 2020 and 2021 was higher than that in other years. Moreover, a general wetting trend has been detected in eastern China during the summer in recent years (Hu et al., 2021), which is largely related to the increase in summer precipitation and decrease in summer potential evapotranspiration. RH had the most significant effect on the 2nd  $O_3$  percentile trends, according to MLR results (Table S2). Therefore, the meteorological component had an inhibitory effect on the increase in the 2nd  $O_3$  percentile trends during May–September 2017–2021. However, owing to the significant emission reduction in  $NO_x$  concentrations, the titration of  $NO_x$  was weakened, and the decrease in  $O_3$  depletion at night led to an increase in the overall 2nd  $O_3$  percentile trends.

Owing to the limitations of the observational data, the analysis of surface  $O_3$  precursors and  $O_3$  formation sensitivity is limited to three cities in eastern China. Although other cities in eastern China were further investigated using satellite observations, TROPOMI only provides observation results for column concentrations at approximately 13:30 LT each day, which did not allow us to obtain diurnal variations in the  $O_3$  formation sensitivity. Further observations must be extended to other cities to investigate the relationship between  $O_3$  and its precursors more comprehensively.

In conclusion, owing to the impact of the COVID-19 pandemic (significant decrease in  $NO_x$  concentrations) and unfavorable meteorological conditions (high relative humidity) in 2020 and 2021 in eastern China, the 98th  $O_3$  percentile concentration in 2020 and 2021 was lower (compared to the 98th  $O_3$  percentile concentration in 2018 and 2019), while the 2nd  $O_3$  percentile concentration showed a rapid upward trend. In addition, the extremely hot and dry meteorological conditions in 2022 increased the 98th and 2nd  $O_3$  percentile concentrations, weakening the decreasing trend in peak  $O_3$  concentrations and increasing the upward trend at low  $O_3$  concentrations.

## 5 Conclusions

In this study, we investigated urban scale O<sub>3</sub> trends in densely populated areas of eastern China using multiple data sources. Through long-term records of surface O<sub>3</sub> and related parameters at 105 urban air quality monitoring sites in eastern China from May to September of 2017 to 2022, we found opposite trends for low and peak surface O<sub>3</sub> concentrations. Statistical results showed that low O<sub>3</sub> concentrations increased significantly (0.06 ppb yr<sup>-1</sup>, 0.3 % yr<sup>-1</sup>), while peak O<sub>3</sub> concentrations decreased considerably (−0.39 ppb yr<sup>-1</sup>, −0.5 % yr<sup>-1</sup>). Anthropogenic emissions were the main driver of both trends, although meteorological effects also played a role.

Based on long-term MAX-DOAS observations in Hefei, Huaibei, and Tai'an, we found that surface O<sub>3</sub> formation sensitivity in the early morning (08:00–09:00 LT) was mainly controlled by VOC concentrations, shifting to an NO<sub>x</sub>-limited regime by midday (12:00–14:00 LT). Moreover, O<sub>3</sub> formation sensitivity is in the VOC-limited regime or transition regime during periods of sharp increases in O<sub>3</sub> concentrations (08:00–11:00 LT) and is usually in the transition or NO<sub>x</sub>-limited regime when O<sub>3</sub> concentration peaks (11:00–14:00 LT). Therefore, the decline in peak O<sub>3</sub> concentrations was attributed to the significant reduction in NO<sub>x</sub> concentrations. To further suppress peak O<sub>3</sub> concentrations and reduce the number of O<sub>3</sub> exceedance days, controlling NO<sub>x</sub> emissions should not be neglected. The increase in low O<sub>3</sub> concentrations can also be attributed to anthropogenic emissions and meteorological effects. Extremely hot and dry conditions can elevate O<sub>3</sub> concentrations by increasing photochemical rates, promoting natural emissions and depressing nighttime O<sub>3</sub> depletion by impairing the wet-scavenging effect. Additionally, a substantial reduction in NO<sub>x</sub> concentrations weakened O<sub>3</sub> titration from fresh NO emissions and increased nighttime O<sub>3</sub> concentrations.

Our results highlight the positive impact of the NO<sub>x</sub> reduction in controlling peak O<sub>3</sub> levels. In response to the current severe O<sub>3</sub> pollution in China, it is crucial to consider the regular transitions in O<sub>3</sub> formation sensitivity throughout the day when formulating O<sub>3</sub> prevention and control policies. When O<sub>3</sub> concentrations are about to peak, a strict control of NO<sub>x</sub> emissions is necessary. This study provides novel insights into the spatiotemporal variability in O<sub>3</sub> formation sensitivity in eastern China and will be further expanded at different altitude levels in our future studies.

**Code availability.** Code related to this paper may be requested from the authors.

**Data availability.** Measurement data in this study are available in the data repository maintained by Mendeley Data at <https://doi.org/10.17632/zd9cb9dk75.1> (Wang, 2024). Real-time

hourly observed urban O<sub>3</sub>, NO<sub>2</sub>, and CO concentrations in 105 cities in eastern China from 2017 to 2022 were obtained from <https://quotsoft.net/air/> (Wang, 2025). TROPOMI data used in this study were obtained from <https://search.earthdata.nasa.gov/search> (NASA, 2025).

**Supplement.** The supplement related to this article is available online at: <https://doi.org/10.5194/acp-25-347-2025-supplement>.

**Author contributions.** CL, CX, and YC conceived and supervised the study. ZW analyzed the data. ZW wrote the paper with input from CL, CX, and YC. CS and HZ reviewed and commented on the paper. All authors contributed to discussing the results and revising the draft.

**Competing interests.** The contact author has declared that none of the authors has any competing interests.

**Disclaimer.** Publisher's note: Copernicus Publications remains neutral with regard to jurisdictional claims made in the text, published maps, institutional affiliations, or any other geographical representation in this paper. While Copernicus Publications makes every effort to include appropriate place names, the final responsibility lies with the authors.

**Acknowledgements.** The authors extend their thanks to editor Jeffrey Geddes and the three reviewers for their time and expertise. We would like to express our gratitude to Fusheng Mou and SuWen Li of Huaibei Normal University for their assistance. We would like to thank the Ministry of Ecology and Environment of China for the O<sub>3</sub>, NO<sub>2</sub>, and CO data. We would like to thank the ERA5 data developers and TROPOMI data developers for providing free and open-source materials.

**Financial support.** This research has been supported by grants from the Anhui Provincial Natural Science Foundation “Jianghuai Meteorological” Joint Fund (grant no. 2208085UQ04), the National Natural Science Foundation of China (grant nos. U21A2027 and 42207113), the Anhui Meteorological Bureau Special Programme for Innovation and Development (grant no. CXB202303), the East China Regional Meteorological Science and Technology Collaborative Innovation Fund (grant no. QYHZ202317), and the China Meteorological Administration “Application of quantum technology in meteorological detection” Youth Innovation Team Project (grant no. CMA2024QN11).

**Review statement.** This paper was edited by Jeffrey Geddes and reviewed by three anonymous referees.

## References

- Bao, J., Li, H., Wu, Z., Zhang, X., Zhang, H., Li, Y., Qian, J., Chen, J., and Deng, L.: Atmospheric carbonyls in a heavy ozone pollution episode at a metropolis in Southwest China: Characteristics, health risk assessment, sources analysis, *J. Environ. Sci.-China*, 113, 40–54, <https://doi.org/10.1016/j.jes.2021.05.029>, 2022.
- Bauwens, M., Verreyken, B., Stavrou, T., Müller, J. F., and Smedt, I. D.: Spaceborne evidence for significant anthropogenic VOC trends in Asian cities over 2005–2019, *Environ. Res. Lett.*, 17, 015008, <https://doi.org/10.1088/1748-9326/ac46eb>, 2022.
- Bloomer, B. J., Stehr, J. W., Piety, C. A., Salawitch, R. J., and Dickerson, R. R.: Observed relationships of ozone air pollution with temperature and emissions, *Geophys. Res. Lett.*, 36, L09803, <https://doi.org/10.1029/2009gl0137308>, 2009.
- Chan, K. L., Wang, S., Liu, C., Zhou, B., Wenig, M. O., and Saiz-Lopez, A.: On the summertime air quality and related photochemical processes in the megacity Shanghai, China, *Sci. Total Environ.*, 580, 974–983, <https://doi.org/10.1016/j.scitotenv.2016.12.052>, 2017.
- Chinese State Council: Action Plan on Air Pollution Prevention and Control, [http://www.gov.cn/zwgg/2013-09/12/content\\_2486773.htm](http://www.gov.cn/zwgg/2013-09/12/content_2486773.htm) (last access: 1 January 2024), 2013 (in Chinese).
- Chinese State Council: Three-Year Action Plan on Defending the Blue Sky, [http://www.gov.cn/zhengce/content/2018-07/03/content\\_5303158.htm](http://www.gov.cn/zhengce/content/2018-07/03/content_5303158.htm) (last access: 1 January 2024), 2018 (in Chinese).
- Churkina, G., Kuik, F., Bonn, B., Lauer, A., Grote, R., Tomiak, K., and Butler, T. M.: Effect of VOC Emissions from Vegetation on Air Quality in Berlin during a Heatwave, *Environ. Sci. Technol.*, 51, 6120–6130, <https://doi.org/10.1021/acs.est.6b06514>, 2017.
- Cooper, O. R., Gao, R. S., Tarasick, D., Leblanc, T., and Sweeney, C.: Long-term ozone trends at rural ozone monitoring sites across the United States, 1990–2010, *J. Geophys. Res.-Atmos.*, 117, D22307, <https://doi.org/10.1029/2012jd018261>, 2012.
- Cynthia Lin, C. Y., Jacob, D. J., Munger, J. W., and Fiore, A. M.: Increasing background ozone in surface air over the United States, *Geophys. Res. Lett.*, 27, 3465–3468, 2000.
- De Smedt, I., Theys, N., Yu, H., Danckaert, T., Lerot, C., Compernelle, S., Van Roozendael, M., Richter, A., Hilboll, A., Peters, E., Pedergnana, M., Loyola, D., Beirle, S., Wagner, T., Eskes, H., van Geffen, J., Boersma, K. F., and Veefkind, P.: Algorithm theoretical baseline for formaldehyde retrievals from S5P TROPOMI and from the QA4ECV project, *Atmos. Meas. Tech.*, 11, 2395–2426, <https://doi.org/10.5194/amt-11-2395-2018>, 2018.
- De Smedt, I., Pinardi, G., Vigouroux, C., Compernelle, S., Bais, A., Benavent, N., Boersma, F., Chan, K.-L., Donner, S., Eichmann, K.-U., Hedelt, P., Hendrick, F., Irie, H., Kumar, V., Lambert, J.-C., Langerock, B., Lerot, C., Liu, C., Loyola, D., PETERS, A., Richter, A., Rivera Cárdenas, C., Romahn, F., Ryan, R. G., Sinha, V., Theys, N., Vlietinck, J., Wagner, T., Wang, T., Yu, H., and Van Roozendael, M.: Comparative assessment of TROPOMI and OMI formaldehyde observations and validation against MAX-DOAS network column measurements, *Atmos. Chem. Phys.*, 21, 12561–12593, <https://doi.org/10.5194/acp-21-12561-2021>, 2021.
- Dimitropoulou, E., Hendrick, F., Pinardi, G., Friedrich, M. M., Merlaud, A., Tack, F., De Longueville, H., Fayt, C., Hermans, C., Laffineur, Q., Fierens, F., and Van Roozendael, M.: Validation of TROPOMI tropospheric NO<sub>2</sub> columns using dual-scan multi-axis differential optical absorption spectroscopy (MAX-DOAS) measurements in Uccle, Brussels, *Atmos. Meas. Tech.*, 13, 5165–5191, <https://doi.org/10.5194/amt-13-5165-2020>, 2020.
- Ding, J., Dai, Q., Fan, W., Lu, M., Zhang, Y., Han, S., and Feng, Y.: Impacts of meteorology and precursor emission change on O<sub>3</sub> variation in Tianjin, China from 2015 to 2021, *J. Environ. Sci.-China*, 126, 506–516, <https://doi.org/10.1016/j.jes.2022.03.010>, 2023.
- Gao, A., Wang, J., Poetzsch, J., Li, S., Gao, B., Wang, P., Luo, J., Fang, X., Li, J., Hu, J., Gao, J., and Zhang, H.: Coordinated health effects attributable to particulate matter and other pollutants exposures in the North China Plain, *Environ. Res.*, 208, 112671, <https://doi.org/10.1016/j.envres.2021.112671>, 2022.
- Garcia, A. R., Volkamer, R., Molina, L. T., Molina, M. J., Samuelson, J., Mellqvist, J., Galle, B., Herndon, S. C., and Kolb, C. E.: Separation of emitted and photochemical formaldehyde in Mexico City using a statistical analysis and a new pair of gas-phase tracers, *Atmos. Chem. Phys.*, 6, 4545–4557, <https://doi.org/10.5194/acp-6-4545-2006>, 2006.
- Gaudel, A., Cooper, O. R., Chang, K.-L., Bourgeois, I., Ziemke, J. R., Strode, S. A., Oman, L. D., Sellitto, P., Nédélec, P., and Blot, R.: Aircraft observations since the 1990s reveal increases of tropospheric ozone at multiple locations across the Northern Hemisphere, *Sci. Adv.*, 6, eaba8272, <https://doi.org/10.1126/sciadv.aba8272>, 2020.
- Guan, Y., Xiao, Y., Rong, B., Zhang, N., and Chu, C.: Long-term health impacts attributable to PM<sub>2.5</sub> and ozone pollution in China's most polluted region during 2015–2020, *J. Clean. Prod.*, 321, 128970, <https://doi.org/10.1016/j.jclepro.2021.128970>, 2021.
- Han, H., Liu, J., Shu, L., Wang, T., and Yuan, H.: Local and synoptic meteorological influences on daily variability in summertime surface ozone in eastern China, *Atmos. Chem. Phys.*, 20, 203–222, <https://doi.org/10.5194/acp-20-203-2020>, 2020.
- Heue, K.-P., Riede, H., Walter, D., Brenninkmeijer, C. A. M., Wagner, T., Frieß, U., Platt, U., Zahn, A., Stratmann, G., and Ziereis, H.: CARIBIC DOAS observations of nitrous acid and formaldehyde in a large convective cloud, *Atmos. Chem. Phys.*, 14, 6621–6642, <https://doi.org/10.5194/acp-14-6621-2014>, 2014.
- Hong, Q., Liu, C., Chan, K. L., Hu, Q., Xie, Z., Liu, H., Si, F., and Liu, J.: Ship-based MAX-DOAS measurements of tropospheric NO<sub>2</sub>, SO<sub>2</sub>, and HCHO distribution along the Yangtze River, *Atmos. Chem. Phys.*, 18, 5931–5951, <https://doi.org/10.5194/acp-18-5931-2018>, 2018.
- Hong, Q., Zhu, L., Xing, C., Hu, Q., Lin, H., Zhang, C., Zhao, C., Liu, T., Su, W., and Liu, C.: Inferring vertical variability and diurnal evolution of O<sub>3</sub> formation sensitivity based on the vertical distribution of summertime HCHO and NO<sub>2</sub> in Guangzhou, China, *Sci. Total Environ.*, 827, 154045, <https://doi.org/10.1016/j.scitotenv.2022.154045>, 2022.
- Hu, W., She, D., Xia, J., He, B., and Hu, C.: Dominant patterns of dryness/wetness variability in the Huang-Huai-Hai River Basin and its relationship with multi-scale climate oscillations, *Atmos. Res.*, 247, 105148, <https://doi.org/10.1016/j.atmosres.2020.105148>, 2021.
- Jacob, D. J., Logan, J. A., and Murti, P. P.: Effect of rising Asian emissions on surface ozone in the United States, *Geophys. Res. Lett.*, 26, 2175–2178, 1999.

- Jin, H., Chen, X., Zhong, R., and Duan, K.: Frequency analysis of extreme precipitation in different regions of the Huaihe River Basin, *Int. J. Climatol.*, 42, 3517–3536, <https://doi.org/10.1002/joc.7430>, 2021.
- Lang, J., Liang, X., Li, S., Zhou, Y., Chen, D., Zhang, Y., and Xu, L.: Understanding the impact of vehicular emissions on air pollution from the perspective of regional transport: A case study of the Beijing-Tianjin-Hebei region in China, *Sci. Total Environ.*, 785, 147304, <https://doi.org/10.1016/j.scitotenv.2021.147304>, 2021.
- Lefohn, A. S., Hazucha, M. J., Shadwick, D., and Adams, W. C.: An alternative form and level of the human health ozone standard, *Inhal. Toxicol.*, 22, 999–1011, 2010.
- Li, J., Lu, K., Lv, W., Li, J., Zhong, L., Ou, Y., Chen, D., Huang, X., and Zhang, Y.: Fast increasing of surface ozone concentrations in Pearl River Delta characterized by a regional air quality monitoring network during 2006–2011, *J. Environ. Sci.-China*, 26, 23–36, [https://doi.org/10.1016/s1001-0742\(13\)60377-0](https://doi.org/10.1016/s1001-0742(13)60377-0), 2014.
- Li, K., Jacob, D. J., Liao, H., Shen, L., Zhang, Q., and Bates, K. H.: Anthropogenic drivers of 2013–2017 trends in summer surface ozone in China, *P. Natl. Acad. Sci. USA*, 116, 422–427, <https://doi.org/10.1073/pnas.1812168116>, 2018.
- Li, K., Jacob, D. J., Shen, L., Lu, X., De Smedt, I., and Liao, H.: Increases in surface ozone pollution in China from 2013 to 2019: anthropogenic and meteorological influences, *Atmos. Chem. Phys.*, 20, 11423–11433, <https://doi.org/10.5194/acp-20-11423-2020>, 2020.
- Li, K., Jacob, D. J., Liao, H., Qiu, Y., Shen, L., Zhai, S., Bates, K. H., Sulprizio, M. P., Song, S., Lu, X., Zhang, Q., Zheng, B., Zhang, Y., Zhang, J., Lee, H. C., and Kuk, S. K.: Ozone pollution in the North China Plain spreading into the late-winter haze season, *P. Natl. Acad. Sci. USA*, 118, e2015797118, <https://doi.org/10.1073/pnas.2015797118>, 2021.
- Li, L., Yang, W., Xie, S., and Wu, Y.: Estimations and uncertainty of biogenic volatile organic compound emission inventory in China for 2008–2018, *Sci. Total Environ.*, 733, 139301, <https://doi.org/10.1016/j.scitotenv.2020.139301>, 2020.
- Li, M., Liu, H., Geng, G., Hong, C., Liu, F., Song, Y., Tong, D., Zheng, B., Cui, H., Man, H., Zhang, Q., and He, K.: Anthropogenic emission inventories in China: a review, *Natl. Sci. Rev.*, 4, 834–866, <https://doi.org/10.1093/nsr/nwx150>, 2017.
- Li, M., Huang, X., Yan, D., Lai, S., Zhang, Z., Zhu, L., Lu, Y., Jiang, X., Wang, N., Wang, T., Song, Y., and Ding, A.: Coping with the concurrent heatwaves and ozone extremes in China under a warming climate, *Sci. Bull.*, 69, 2938–2947, <https://doi.org/10.1016/j.scib.2024.05.034>, 2024.
- Li, X.-B., Yuan, B., Parrish, D. D., Chen, D., Song, Y., Yang, S., Liu, Z., and Shao, M.: Long-term trend of ozone in southern China reveals future mitigation strategy for air pollution, *Atmos. Environ.*, 269, 118869, <https://doi.org/10.1016/j.atmosenv.2021.118869>, 2022.
- Li, X., Ren, J., Huang, R., Chen, L., Li, Y., Qiao, X., Cheng, Y., Zhao, B., Yin, D., Gao, D., Sun, Y., and Zhang, F.: The Aggravation of Summertime Nocturnal Ozone Pollution in China and Its Potential Impact on the Trend of Nitrate Aerosols, *Geophys. Res. Lett.*, 50, e2023GL103242, <https://doi.org/10.1029/2023gl103242>, 2023.
- Lin, H., Xing, C., Hong, Q., Liu, C., Ji, X., Liu, T., Lin, J., Lu, C., Tan, W., Li, Q., and Liu, H.: Diagnosis of Ozone Formation Sensitivities in Different Height Layers via MAX-DOAS Observations in Guangzhou, *J. Geophys. Res.-Atmos.*, 127, e2022JD036803, <https://doi.org/10.1029/2022jd036803>, 2022.
- Lin, N., Wang, Y., Zhang, Y., and Yang, K.: A large decline of tropospheric NO<sub>2</sub> in China observed from space by SNPP OMPS, *Sci. Total Environ.*, 675, 337–342, <https://doi.org/10.1016/j.scitotenv.2019.04.090>, 2019.
- Liu, C., Hu, Q., Zhang, C., Xia, C., Yin, H., Su, W., Wang, X., Xu, Y., and Zhang, Z.: First Chinese ultraviolet–visible hyperspectral satellite instrument implicating global air quality during the COVID-19 pandemic in early 2020, *Light: Science & Applications*, 11, 28, <https://doi.org/10.1038/s41377-022-00722-x>, 2022a.
- Liu, C., Xing, C., Hu, Q., Li, Q., Liu, H., Hong, Q., Tan, W., Ji, X., Lin, H., Lu, C., Lin, J., Liu, H., Wei, S., Chen, J., Yang, K., Wang, S., Liu, T., and Chen, Y.: Ground-Based Hyperspectral Stereoscopic Remote Sensing Network: A Promising Strategy to Learn Coordinated Control of O<sub>3</sub> and PM<sub>2.5</sub> over China, *Engineering*, 19, 71–83, <https://doi.org/10.1016/j.eng.2021.02.019>, 2022b.
- Liu, J., Wang, S., Zhang, Y., Yan, Y., Zhu, J., Zhang, S., Wang, T., Tan, Y., and Zhou, B.: Investigation of formaldehyde sources and its relative emission intensity in shipping channel environment, *J. Environ. Sci.-China*, 142, 142–154, <https://doi.org/10.1016/j.jes.2023.06.020>, 2024.
- Liu, Y., Geng, G., Cheng, J., Liu, Y., Xiao, Q., Liu, L., Shi, Q., Tong, D., He, K., and Zhang, Q.: Drivers of Increasing Ozone during the Two Phases of Clean Air Actions in China 2013–2020, *Environ. Sci. Technol.*, 57, 8954–8964, <https://doi.org/10.1021/acs.est.3c00054>, 2023.
- Lu, C., Li, Q., Xing, C., Hu, Q., Tan, W., Lin, J., Zhang, Z., Tang, Z., Cheng, J., Chen, A., and Liu, C.: Identification of O<sub>3</sub> Sensitivity to Secondary HCHO and NO<sub>2</sub> Measured by MAX-DOAS in Four Cities in China, *Remote Sens.*, 16, 662, <https://doi.org/10.3390/rs16040662>, 2024.
- Lu, X., Zhang, L., Wang, X., Gao, M., Li, K., Zhang, Y., Yue, X., and Zhang, Y.: Rapid Increases in Warm-Season Surface Ozone and Resulting Health Impact in China Since 2013, *Environ. Sci. Tech. Lett.*, 7, 240–247, <https://doi.org/10.1021/acs.estlett.0c00171>, 2020.
- Ma, Y., Diao, Y., Zhang, B., Wang, W., Ren, X., Yang, D., Wang, M., Shi, X., and Zheng, J.: Detection of formaldehyde emissions from an industrial zone in the Yangtze River Delta region of China using a proton transfer reaction ion-drift chemical ionization mass spectrometer, *Atmos. Meas. Tech.*, 9, 6101–6116, <https://doi.org/10.5194/amt-9-6101-2016>, 2016.
- Ma, Z., Liu, C., Zhang, C., Liu, P., Ye, C., Xue, C., Zhao, D., Sun, J., Du, Y., Chai, F., and Mu, Y.: The levels, sources and reactivity of volatile organic compounds in a typical urban area of Northeast China, *J. Environ. Sci.-China*, 79, 121–134, <https://doi.org/10.1016/j.jes.2018.11.015>, 2019.
- MacDonald, S. M., Oetjen, H., Mahajan, A. S., Whalley, L. K., Edwards, P. M., Heard, D. E., Jones, C. E., and Plane, J. M. C.: DOAS measurements of formaldehyde and glyoxal above a south-east Asian tropical rainforest, *Atmos. Chem. Phys.*, 12, 5949–5962, <https://doi.org/10.5194/acp-12-5949-2012>, 2012.
- Mousavinezhad, S., Choi, Y., Pouyaei, A., Ghahremanloo, M., and Nelson, D. L.: A comprehensive investigation of surface ozone pollution in China, 2015–2019: Separating the contributions from meteorology and precursor emissions, *Atmos. Res.*, 257, 105599, <https://doi.org/10.1016/j.atmosres.2021.105599>, 2021.

- NASA: Earthdata Search, <https://search.earthdata.nasa.gov/search>, last access: 5 January 2025.
- Possanzini, M., Di Palo, V., and Cecinato, A.: Sources and photodecomposition of formaldehyde and acetaldehyde in Rome ambient air, *Atmos. Environ.*, 36, 3195–3201, 2002.
- Ren, B., Xie, P., Xu, J., Li, A., Qin, M., Hu, R., Zhang, T., Fan, G., Tian, X., Zhu, W., Hu, Z., Huang, Y., Li, X., Meng, F., Zhang, G., Tong, J., Ren, H., Zheng, J., Zhang, Z., and Lv, Y.: Vertical characteristics of NO<sub>2</sub> and HCHO, and the ozone formation regimes in Hefei, China, *Sci. Total Environ.*, 823, 153425, <https://doi.org/10.1016/j.scitotenv.2022.153425>, 2022.
- Ren, J., Guo, F., and Xie, S.: Diagnosing ozone–NO<sub>x</sub>–VOC sensitivity and revealing causes of ozone increases in China based on 2013–2021 satellite retrievals, *Atmos. Chem. Phys.*, 22, 15035–15047, <https://doi.org/10.5194/acp-22-15035-2022>, 2022.
- Song, Y., Xing, C., Liu, C., Lin, J., Wu, H., Liu, T., Lin, H., Zhang, C., Tan, W., Ji, X., Liu, H., and Li, Q.: Evaluation of transport processes over North China Plain and Yangtze River Delta using MAX-DOAS observations, *Atmos. Chem. Phys.*, 23, 1803–1824, <https://doi.org/10.5194/acp-23-1803-2023>, 2023.
- Su, W., Liu, C., Hu, Q., Fan, G., Xie, Z., Huang, X., Zhang, T., Chen, Z., Dong, Y., Ji, X., Liu, H., Wang, Z., and Liu, J.: Characterization of ozone in the lower troposphere during the 2016 G20 conference in Hangzhou, *Sci. Rep.*, 7, 17368, <https://doi.org/10.1038/s41598-017-17646-x>, 2017.
- Sun, X., Zhao, T., Bai, Y., Kong, S., Zheng, H., Hu, W., Ma, X., and Xiong, J.: Meteorology impact on PM<sub>2.5</sub> change over a receptor region in the regional transport of air pollutants: observational study of recent emission reductions in central China, *Atmos. Chem. Phys.*, 22, 3579–3593, <https://doi.org/10.5194/acp-22-3579-2022>, 2022.
- Sun, Y., Yin, H., Liu, C., Zhang, L., Cheng, Y., Palm, M., Notholt, J., Lu, X., Vigouroux, C., Zheng, B., Wang, W., Jones, N., Shan, C., Qin, M., Tian, Y., Hu, Q., Meng, F., and Liu, J.: Mapping the drivers of formaldehyde (HCHO) variability from 2015 to 2019 over eastern China: insights from Fourier transform infrared observation and GEOS-Chem model simulation, *Atmos. Chem. Phys.*, 21, 6365–6387, <https://doi.org/10.5194/acp-21-6365-2021>, 2021.
- Taguchi, S., Hagiwara, M., Shibata, A., Fujinari, H., Matsumoto, S., Kuwata, M., Sazawa, K., Hata, N., and Kuramitz, H.: Investigation and modeling of diurnal variation in suburban ambient formaldehyde concentration, *Environ. Sci. Pollut. R.*, 28, 13425–13438, <https://doi.org/10.1007/s11356-020-11465-w>, 2020.
- van Geffen, J., Boersma, K. F., Eskes, H., Sneep, M., ter Linden, M., Zara, M., and Veefkind, J. P.: S5P TROPOMI NO<sub>2</sub> slant column retrieval: method, stability, uncertainties and comparisons with OMI, *Atmos. Meas. Tech.*, 13, 1315–1335, <https://doi.org/10.5194/amt-13-1315-2020>, 2020.
- Veefkind, J. P., Aben, I., McMullan, K., Förster, H., de Vries, J., Otter, G., Claas, J., Eskes, H. J., de Haan, J. F., Kleipool, Q., van Weele, M., Hasekamp, O., Hoogeveen, R., Landgraf, J., Snel, R., Tol, P., Ingmann, P., Voors, R., Kruizinga, B., Vink, R., Visser, H., and Levelt, P. F.: TROPOMI on the ESA Sentinel-5 Precursor: A GMES mission for global observations of the atmospheric composition for climate, air quality and ozone layer applications, *Remote Sens. Environ.*, 120, 70–83, <https://doi.org/10.1016/j.rse.2011.09.027>, 2012.
- Wang, M., Chen, W., Shao, M., Lu, S., Zeng, L., and Hu, M.: Investigation of carbonyl compound sources at a rural site in the Yangtze River Delta region of China, *J. Environ. Sci.-China*, 28, 128–136, <https://doi.org/10.1016/j.jes.2014.12.001>, 2015.
- Wang, N., Lyu, X., Deng, X., Huang, X., Jiang, F., and Ding, A.: Aggravating O<sub>3</sub> pollution due to NO<sub>x</sub> emission control in eastern China, *Sci. Total Environ.*, 677, 732–744, <https://doi.org/10.1016/j.scitotenv.2019.04.388>, 2019.
- Wang, W., Parrish, D. D., Wang, S., Bao, F., Ni, R., Li, X., Yang, S., Wang, H., Cheng, Y., and Su, H.: Long-term trend of ozone pollution in China during 2014–2020: distinct seasonal and spatial characteristics and ozone sensitivity, *Atmos. Chem. Phys.*, 22, 8935–8949, <https://doi.org/10.5194/acp-22-8935-2022>, 2022.
- Wang, X.: Air Quality and Weather, <https://quotsoft.net/air/>, last access: 5 January 2025.
- Wang, Y., Yang, X., Wu, K., Mei, H., De Smedt, I., Wang, S., Fan, J., Lyu, S., and He, C.: Long-term trends of ozone and precursors from 2013 to 2020 in a megacity (Chengdu), China: Evidence of changing emissions and chemistry, *Atmos. Res.*, 278, 106309, <https://doi.org/10.1016/j.atmosres.2022.106309>, 2022.
- Wang, Y., Jiang, S., Huang, L., Lu, G., Kasemsan, M., Yaluk, E. A., Liu, H., Liao, J., Bian, J., Zhang, K., Chen, H., and Li, L.: Differences between VOCs and NO<sub>x</sub> transport contributions, their impacts on O<sub>3</sub>, and implications for O<sub>3</sub> pollution mitigation based on CMAQ simulation over the Yangtze River Delta, China, *Sci. Total Environ.*, 872, 162118, <https://doi.org/10.1016/j.scitotenv.2023.162118>, 2023a.
- Wang, Y., Zhao, Y., Liu, Y., Jiang, Y., Zheng, B., Xing, J., Liu, Y., Wang, S., and Nielsen, C. P.: Sustained emission reductions have restrained the ozone pollution over China, *Nat. Geosci.*, 16, 967–974, <https://doi.org/10.1038/s41561-023-01284-2>, 2023b.
- Wang, Z.: Opposing trends in the peak and low ozone concentrations in eastern China: Anthropogenic and meteorological influences, Version V1, Mendeley Data [data set], <https://doi.org/10.17632/zd9cb9dk75.1>, 2024.
- Wang, Z., Liu, C., Xie, Z., Hu, Q., Andreae, M. O., Dong, Y., Zhao, C., Liu, T., Zhu, Y., Liu, H., Xing, C., Tan, W., Ji, X., Lin, J., and Liu, J.: Elevated dust layers inhibit dissipation of heavy anthropogenic surface air pollution, *Atmos. Chem. Phys.*, 20, 14917–14932, <https://doi.org/10.5194/acp-20-14917-2020>, 2020.
- Wang, Z., Shi, C., Zhang, H., Chen, Y., Chi, X., Xia, C., Wang, S., Zhu, Y., Zhang, K., Chen, X., Xing, C., and Liu, C.: Measurement report: Dust and anthropogenic aerosols’ vertical distributions over northern China dense aerosols gathered at the top of the mixing layer, *Atmos. Chem. Phys.*, 23, 14271–14292, <https://doi.org/10.5194/acp-23-14271-2023>, 2023.
- Weng, X., Forster, G. L., and Nowack, P.: A machine learning approach to quantify meteorological drivers of ozone pollution in China from 2015 to 2019, *Atmos. Chem. Phys.*, 22, 8385–8402, <https://doi.org/10.5194/acp-22-8385-2022>, 2022.
- Wood, E. C., Canagaratna, M. R., Herndon, S. C., Onasch, T. B., Kolb, C. E., Worsnop, D. R., Kroll, J. H., Knighton, W. B., Seila, R., Zavala, M., Molina, L. T., DeCarlo, P. F., Jimenez, J. L., Weinheimer, A. J., Knapp, D. J., Jobson, B. T., Stutz, J., Kuster, W. C., and Williams, E. J.: Investigation of the correlation between odd oxygen and secondary organic aerosol in Mexico City and Houston, *Atmos. Chem. Phys.*, 10, 8947–8968, <https://doi.org/10.5194/acp-10-8947-2010>, 2010.

- Wu, Y., Chen, W., You, Y., Xie, Q., Jia, S., and Wang, X.: Quantitative impacts of vertical transport on the long-term trend of nocturnal ozone increase over the Pearl River Delta region during 2006–2019, *Atmos. Chem. Phys.*, 23, 453–469, <https://doi.org/10.5194/acp-23-453-2023>, 2023.
- Xing, C., Liu, C., Hong, Q., Liu, H., Wu, H., Lin, J., Song, Y., Chen, Y., Liu, T., Hu, Q., Tan, W., and Lin, H.: Vertical distributions and potential sources of wintertime atmospheric pollutants and the corresponding ozone production on the coast of Bohai Sea, *J. Environ. Manage.*, 319, 115721, <https://doi.org/10.1016/j.jenvman.2022.115721>, 2022.
- Xing, C., Liu, C., Lin, J., Tan, W., and Liu, T.: VOCs hyperspectral imaging: A new insight into evaluate emissions and the corresponding health risk from industries, *J. Hazard. Mater.*, 461, 132573, <https://doi.org/10.1016/j.jhazmat.2023.132573>, 2024.
- Xue, J., Zhao, T., Luo, Y., Miao, C., Su, P., Liu, F., Zhang, G., Qin, S., Song, Y., Bu, N., and Xing, C.: Identification of ozone sensitivity for NO<sub>2</sub> and secondary HCHO based on MAX-DOAS measurements in northeast China, *Environ. Int.*, 160, 107048, <https://doi.org/10.1016/j.envint.2021.107048>, 2022.
- Zhai, S., Jacob, D. J., Wang, X., Shen, L., Li, K., Zhang, Y., Gui, K., Zhao, T., and Liao, H.: Fine particulate matter (PM<sub>2.5</sub>) trends in China, 2013–2018: separating contributions from anthropogenic emissions and meteorology, *Atmos. Chem. Phys.*, 19, 11031–11041, <https://doi.org/10.5194/acp-19-11031-2019>, 2019.
- Zhang, Q., Zheng, Y., Tong, D., Shao, M., Wang, S., Zhang, Y., Xu, X., Wang, J., He, H., Liu, W., Ding, Y., Lei, Y., Li, J., Wang, Z., Zhang, X., Wang, Y., Cheng, J., Liu, Y., Shi, Q., Yan, L., Geng, G., Hong, C., Li, M., Liu, F., Zheng, B., Cao, J., Ding, A., Gao, J., Fu, Q., Huo, J., Liu, B., Liu, Z., Yang, F., He, K., and Hao, J.: Drivers of improved PM<sub>2.5</sub> air quality in China from 2013 to 2017, *P. Natl. Acad. Sci. USA*, 116, 24463–24469, <https://doi.org/10.1073/pnas.1907956116>, 2019.
- Zhang, T., Tam, C.-Y., Lau, N.-C., Wang, J., Yang, S., Chen, J., Yu, W., Jiang, X., and Gao, P.: Influences of the boreal winter Arctic Oscillation on the peak-summer compound heat waves over the Yangtze–Huaihe River basin: the North Atlantic capacitor effect, *Clim. Dynam.*, 59, 2331–2343, <https://doi.org/10.1007/s00382-022-06212-5>, 2022.
- Zhang, T., Deng, Y., Chen, J., Yang, S., and Dai, Y.: An energetics tale of the 2022 mega-heatwave over central-eastern China, *npj Clim. Atmos. Sci.*, 6, 162, <https://doi.org/10.1038/s41612-023-00490-4>, 2023.
- Zhang, W., Pan, S., Cao, L., Cai, X., Zhang, K., Xu, Y., and Xu, W.: Changes in extreme climate events in eastern China during 1960–2013: A case study of the Huaihe River Basin, *Quatern. Int.*, 380–381, 22–34, <https://doi.org/10.1016/j.quaint.2014.12.038>, 2015.
- Zhang, X., Xu, W., Zhang, G., Lin, W., Zhao, H., Ren, S., Zhou, G., Chen, J., and Xu, X.: First long-term surface ozone variations at an agricultural site in the North China Plain: Evolution under changing meteorology and emissions, *Sci. Total Environ.*, 860, 160520, <https://doi.org/10.1016/j.scitotenv.2022.160520>, 2023.
- Zhang, Y.-L. and Cao, F.: Fine particulate matter (PM<sub>2.5</sub>) in China at a city level, *Sci. Rep.*, 5, 14884, <https://doi.org/10.1038/srep14884>, 2015.
- Zheng, B., Tong, D., Li, M., Liu, F., Hong, C., Geng, G., Li, H., Li, X., Peng, L., Qi, J., Yan, L., Zhang, Y., Zhao, H., Zheng, Y., He, K., and Zhang, Q.: Trends in China’s anthropogenic emissions since 2010 as the consequence of clean air actions, *Atmos. Chem. Phys.*, 18, 14095–14111, <https://doi.org/10.5194/acp-18-14095-2018>, 2018.